

# Temporal Specification and Bilaterality of Human Neocortical Topographic Gene Expression

Mihovil Pletikos,<sup>1,2,5</sup> André M.M. Sousa,<sup>1,3,5</sup> Goran Sedmak,<sup>1,2,5</sup> Kyle A. Meyer,<sup>1</sup> Ying Zhu,<sup>1</sup> Feng Cheng,<sup>1,4</sup> Mingfeng Li,<sup>1</sup> Yuka Imamura Kawasawa,<sup>1</sup> and Nenad Sestan<sup>1,\*</sup>

<sup>1</sup>Department of Neurobiology and Kavli Institute for Neuroscience, Yale School of Medicine, New Haven, CT 06510, USA

<sup>2</sup>Graduate Program in Neuroscience, School of Medicine, University of Zagreb, 10000 Zagreb, Croatia

<sup>3</sup>Graduate Program in Areas of Basic and Applied Biology, Abel Salazar Biomedical Sciences Institute, University of Porto, 4099-003 Porto, Portugal

<sup>4</sup>Department of Pharmaceutical Sciences, College of Pharmacy, University of South Florida, Tampa, FL 33612, USA

<sup>5</sup>These authors contributed equally to this work

\*Correspondence: [nenad.sestan@yale.edu](mailto:nenad.sestan@yale.edu)

<http://dx.doi.org/10.1016/j.neuron.2013.11.018>

## SUMMARY

Transcriptional events involved in the development of human cerebral neocortex are poorly understood. Here, we analyzed the temporal dynamics and laterality of gene expression in human and macaque monkey neocortex. We found that interareal differences exhibit a temporal hourglass pattern, dividing the human neocortical development into three major phases. The first phase, corresponding to prenatal development, is characterized by the highest number of differential expressed genes among areas and gradient-like expression patterns, including those that are different between human and macaque. The second, preadolescent phase, is characterized by lesser interareal expression differences and by an increased synchronization of areal transcriptomes. During the third phase, from adolescence onward, differential expression among areas increases again driven predominantly by a subset of areas, without obvious gradient-like patterns. Analyses of left-right gene expression revealed population-level global symmetry throughout the fetal and postnatal time span. Thus, human neocortical topographic gene expression is temporally specified and globally symmetric.

## INTRODUCTION

The cerebral neocortex (NCX) is organized into functionally distinct sensory, motor, and association areas that provide the biological substrates underlying perception, behavior, and cognition (Brodmann, 1909; O'Leary and Sahara, 2008; Rakic, 1988; Rash and Grove, 2006; Sur and Rubenstein, 2005). While the basic architecture of this areal map is shared among mammals, important species-specific organizational differences have allowed for the elaboration of human-specific cognition and behavior (Hill et al., 2010; Judaš et al., 2013; Kaas, 2012; Kennedy and Dehay, 2012; Lui et al., 2011; Molnár and Clowry, 2012; Preuss, 2011).

Another key feature of the human NCX is that it covers the surface of the left and right hemispheres, each comprising a topographically matched, though slightly structurally and functionally asymmetric areal map (Amunts et al., 2003; Gazzaniga et al., 1962; Geschwind and Levitsky, 1968). This asymmetric organization plays a crucial role in functional lateralization of many cognitive and motor functions, such as language and handedness, between the hemispheres. Several lines of evidence indicate that these asymmetries are reflected at the molecular (Sun et al., 2005) and cellular (Amunts et al., 2003; Hayes and Lewis, 1993) levels. Structural asymmetry first appears during the late midfetal period (Chi et al., 1977; Kasprian et al., 2011) and becomes more prominent during early postnatal development when functional asymmetries become noticeable (Amunts et al., 2003; Hill et al., 2010).

Multiple lines of evidence indicate that distinct human neocortical areas, and the hemispheres as a whole, mature at different rates (Flechsig, 1901; Giedd et al., 1999; Giedd and Rapoport, 2010; Huttenlocher and Dabholkar, 1997; Sowell et al., 2003). For example, axons in primary sensory-motor areas start to myelinate before those in the association areas (Flechsig, 1901). Other processes such as synaptogenesis also exhibit prominent interareal differences in their maturational trajectories (Huttenlocher and Dabholkar, 1997). Furthermore, the right hemisphere appears to mature faster than the left during late fetal and early postnatal development (Taylor, 1969; Thatcher et al., 1987).

There is increasing evidence to suggest that processes regulating areal patterning and asymmetry, as well as the maturational trajectories of these processes, are affected in major psychiatric and neurological disorders (Cullen et al., 2006; Faludi and Mirnics, 2011; Piao et al., 2004; Rapoport and Gogtay, 2008). Moreover, the progression of certain neuropathologies follows a stereotypic areal pattern (Braak et al., 1993), indicating that the mechanisms involved in patterning and asymmetry may play a role in the manifestation of disease. However, little is known about these developmental processes in normal or diseased human brains, or how they differ among mammals, especially closely related nonhuman primates (NHPs).

Gene expression has previously been profiled in the developing human NCX (Abrahams et al., 2007; Colantuoni et al., 2011; Ip et al., 2010; Johnson et al., 2009; Kang et al., 2011;

Lambert et al., 2011; Sun et al., 2005). However, most of these studies were restricted to a small number of areas and time points. Furthermore, a number of genes was found to be expressed asymmetrically in the early fetal (Sun et al., 2005) NCX, but not in midfetal or adult NCX (Hawrylycz et al., 2012; Johnson et al., 2009; Lambert et al., 2011), suggesting that transcriptional asymmetry may be temporally regulated. In the present study, we analyzed the temporal dynamics and left-right asymmetry of NCX topographic gene expression across the full course of fetal and postnatal development and adulthood.

## RESULTS

### Interareal Transcriptional Divergence Exhibits a Temporal Hourglass Pattern

Our previous analyses of gene expression in the human brain revealed robust transcriptional differences among topographically defined areas of the fetal and, to a lesser extent, adult NCX (Johnson et al., 2009; Kang et al., 2011). To analyze temporal progression and left-right asymmetry of areal gene expression, we performed a secondary analysis of this data set (Kang et al., 2011) that included 11 topographically defined NCX areas corresponding to the orbital (OFC), dorsolateral (DFC), ventrolateral (VFC), medial (MFC), and primary motor (M1C) cortices of the frontal lobe; the primary somatosensory (S1C) and posterior inferior (IPC) cortices of the parietal lobe; the primary auditory (A1C), posterior superior (STC), and anterior inferior (ITC) cortices of the temporal lobe; and the primary visual (V1C) cortex of the occipital lobe (Figure 1 and Supplemental Experimental Procedures, Note 2 for topographic sampling, available online). This data set was generated using 886 tissue samples isolated from left and right hemispheres of 53 clinically unremarkable postmortem human brain specimens spanning from early fetal development through old age (from 10 weeks of postconception [PCW] to 82 years of age), which corresponded to periods 3–15, as previously designated, an interval during which all of the analyzed putative functional areas were represented (Kang et al., 2011) (Tables S1A and S2).

The areal localization of dissected NCX samples was previously verified by histology in the postnatal brains and matched across fetal periods using the same anatomical landmarks (Supplemental Experimental Procedures, Note 2; see also Kang et al., 2011). A hierarchical clustering of both fetal and postnatal NCX samples confirmed their grouping by topographical proximity and functional overlap (Figure 2A). Principal component analysis also revealed that transcriptional differences across periods account for the majority of the variance among NCX samples (Figure S1A), indicating that NCX areal gene expression is strongly developmentally regulated.

To investigate how putative areal transcriptional differences change over time, we used ANOVA to identify genes that exhibit differential expression (DEX) among areas in each period (henceforth referred to as the interareal divergence; Supplemental Experimental Procedures, Note 3.3). This analysis revealed that interareal transcriptional divergence, but not the total number of expressed genes, exhibits a previously unrecognized temporal hourglass pattern, with robust and dynamic differences

found prenatally and, to a lesser extent from adolescence onward, with few in infancy and childhood (Figures 2B and S1B). In contrast, differential expression among other (non-neocortical) brain regions did not exhibit the same temporal hourglass pattern (Figure S1B).

We also analyzed the genotype of individuals using the data previously generated using Illumina HumanOmni 2.5 SNP arrays (Kang et al., 2011) to test whether the hourglass pattern could be explained by a reduction in the genetic diversity among individuals in periods 8 to 11. We observed that the genetic diversity of samples varies throughout development in a random way, without any observable pattern for periods 8 to 11 compared with others. We also found no relation with the number of samples (Figure S1C).

To estimate the contribution of differences in specific putative areas to the overall interareal divergence, Tukey's pairwise comparison was performed after ANOVA to determine the total number of significant ( $p < 0.01$ ) DEX gene comparisons of each area with all the other areas for a given period. The relative contribution of areas to the overall hourglass shape varied across periods. During fetal periods, MFC, ITC, and the primary areas (V1C, A1C, S1C, and M1C) exhibited the most prominent dissimilarity, whereas only MFC and V1C showed robust dissimilarities during adolescence and adulthood (Figure 2C). Together, these findings show that the pattern of interareal transcriptional divergence is specified over time and exhibits an hourglass pattern, with infancy and childhood representing a long phase of minimal divergence. Our results also show that the spatial pattern of interareal divergence is mainly driven by a subset of putative functional areas.

### Temporal Transcriptional Hourglass Pattern Reflects Putative Areal and Functional Differences

We hypothesized that increased interareal transcriptional divergence during fetal development and from adolescence onward reflects the differences in the underlying molecular and cellular processes between these two phases. Consistent with this hypothesis, only 848 of 3,125 (27%) interareal DEX genes were DEX both in fetal development and from adolescence onward. To gain insights into the differential organization of the NCX transcriptomes during the two phases of increased interareal differences, we performed weighted gene coexpression network analysis (Supplemental Experimental Procedures, Note 3.7) to identify modules of coexpressed genes with often-shared functional relevance. Within fetal development, we identified 122 modules (M1–M122; Table S4A), and from adolescence on we found 207 modules (M123–M329; Table S4B). Functional annotation of the modules revealed significant differences between the organization of fetal and adolescent/adult differential putative areal transcriptomes. Furthermore, the gene ontology (GO) enrichment analysis (Supplemental Experimental Procedures, Note 3.8) revealed significant differences between fetal and adolescent/adult DEX and also between coexpression modules in the enrichment for GO categories (Tables S3 and S4). Among exclusively fetal GO categories were mostly categories related with developmental processes, such as phosphoprotein, neuron differentiation, cell cycle, neuron development, cell morphogenesis, mitosis, cell morphogenesis

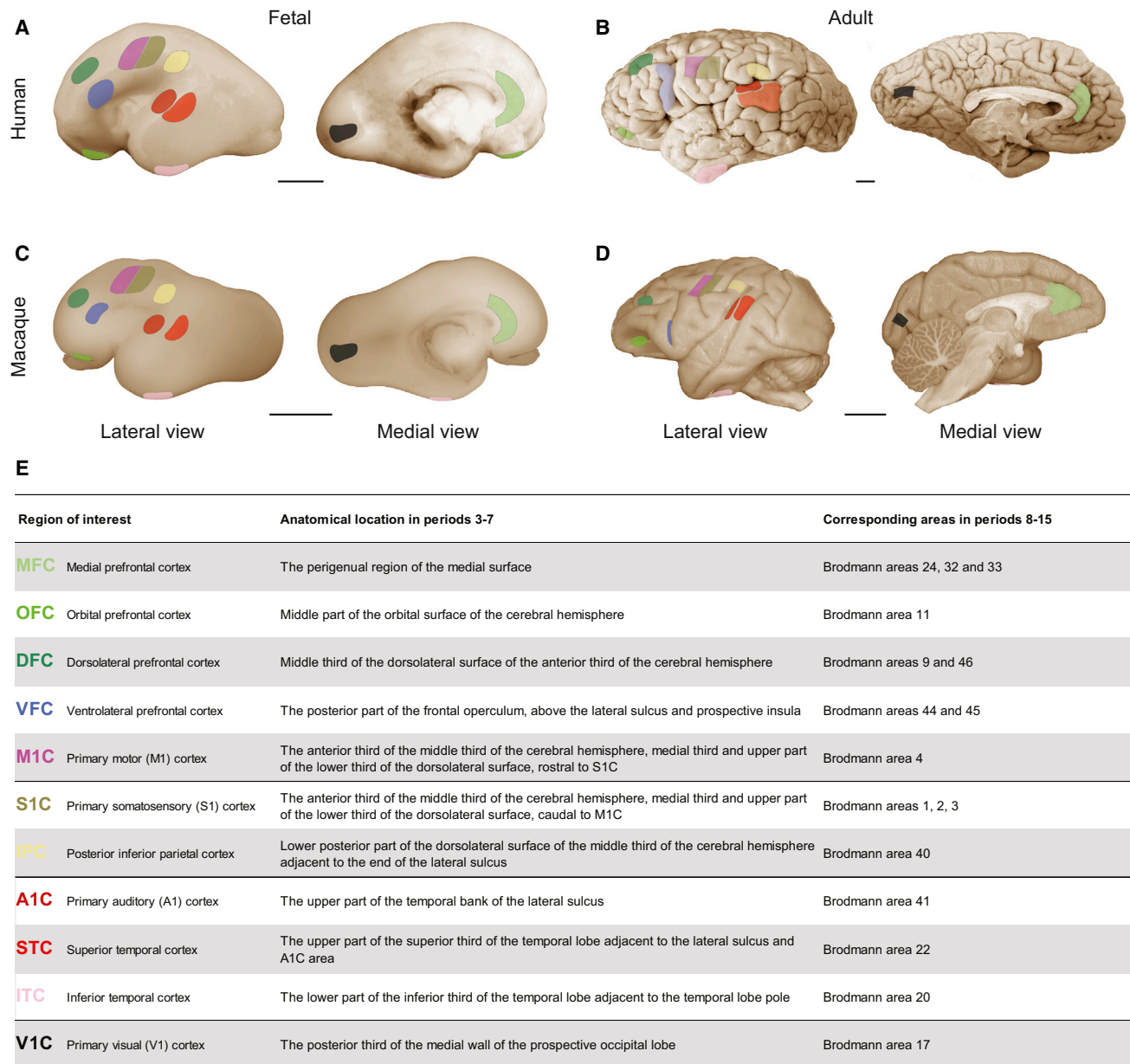


**Figure 1. Topographic Locations of NCX Samples in the Fetal and Adult Human and Macaque Brains**

Schematic shows anatomical positions of dissections of NCX samples in prenatal (A) and postnatal (B) human and prenatal (C) and postnatal (D) macaque brains, and their corresponding Brodmann areas in the postnatal NCX (E). Each NCX sample is colored by the same color in all figures of this article. Scale bar represents 1 cm. See also [Tables S1](#) and [S2](#).

involved in neuron differentiation, cell adhesion, and cellular component morphogenesis (Bonferroni adjusted  $p \leq 6.61 \times 10^{-11}$  per category; [Table S3A](#)). In contrast, exclusively adolescent and adult GO categories were mostly related to processes associated with neuronal and synaptic function, including synaptic vesicle, transport, domain:C2 1 and 2, intrinsic to plasma membrane, intrinsic to membrane, clathrin-coated vesicle, neurological system process, neurotransmitter binding, coated vesicle, integral to membrane, and monovalent

inorganic cation transport (Bonferroni adjusted  $p \leq 2.39 \times 10^{-6}$  per category; [Table S3C](#)).

Many fetal coexpression modules had pronounced gradients and/or well-defined compartments with distinct boundaries ([Figures 3A–3H](#)). In addition to expected gradients with prefrontal/frontal-enriched graded expression along the anterior-posterior axis (e.g., M54, M62, M80, and M91), we found patterns including those with temporal (e.g., M2 and M13), occipital (e.g., M105), occipitotemporal (e.g., M5), perisylvian

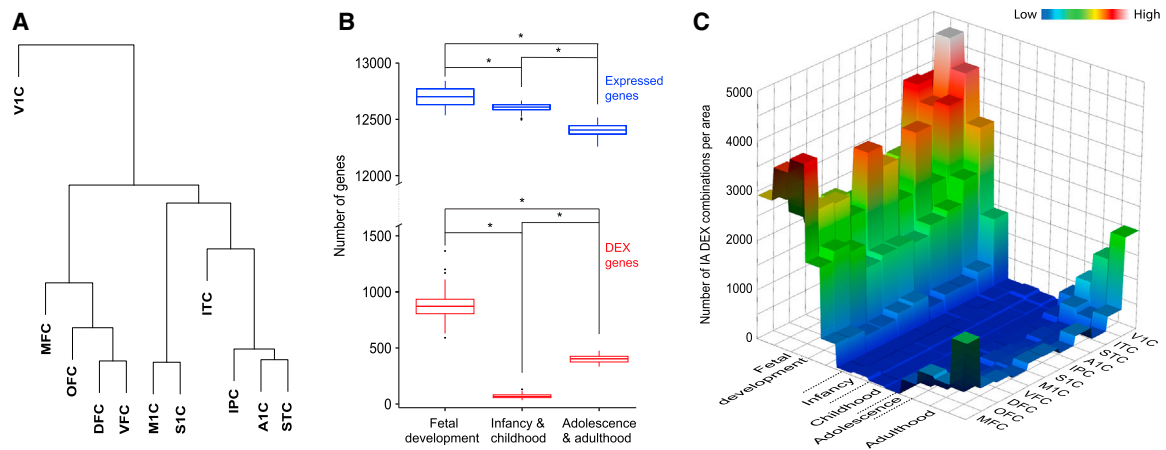


**Figure 2. Neocortical Interareal Differences in Gene Expression Exhibit a Temporal Hourglass Pattern**

(A) Unsupervised hierarchical clustering of the 11 NCX areas profiled in this study, based on the transcriptome of each area from the period of fetal development throughout life, showing relative transcriptional differences.

(B) Boxplots of subsampling permutations show the number of expressed (blue) and differentially expressed (red) genes among neocortical areas across fetal development (periods 3–7), infancy (periods 8 and 9), childhood (periods 10 and 11), adolescence (period 12), and adulthood (periods 13–15). Boxes represent the 25<sup>th</sup> and 75<sup>th</sup> percentiles. Whiskers represent the extension from the 25<sup>th</sup> and 75<sup>th</sup> percentile to the lowest or highest value, respectively, that is within 1.5 interquartile range.

(C) Post hoc Tukey tests were used to identify significant interareal (IA) DEX combinations. A 3D heatmap shows the number of IA DEX combinations per NCX area over time. See also [Figure S1](#) and [Table S3](#).

(e.g., M118), and ventromedial areas (MFC, OFC, and V1C; e.g., M100). The majority of the modules exhibited temporally specified areal patterns that changed dramatically across fetal periods and lost their prominent areal differences postnatally ([Figures S2A–S2H](#) and also see [Tables S4A](#) and [S4B](#) with the list of modules with spatiotemporal patterns). Areal expression patterns of six selected intramodular hub genes were successfully validated by quantitative RT-PCR (qRT-PCR; median correlation with the array data,  $r = 0.88$ ; [Figures 3I–3L](#) and [S3A–S3L](#)). *CLMP*, a gene encoding an adhesion molecule ([Figures 3I](#), [S3A](#), and [S3B](#)), and *WNT7B*, a gene involved in early brain development and dendritic arborization ([Harrison-Uy and Pleasure, 2012](#)) ([Figures 3K](#), [S3I](#), and [S3J](#)), displayed expression gradients along the rostrocaudal axis in anterior-posterior and posterior-anterior directions, respectively. We also validated genes with enriched expression in the temporal lobe areas, such as *NR2F2* (*COUP-TF2*) ([Figure 3L](#), [S3C](#), and [S3D](#)), a gene enriched in the caudal ganglionic eminence and involved in migration of interneurons ([Tripodi et al., 2004](#)), or restricted to the putative temporal lobe areas, including the previously uncharacterized gene *C13ORF38* ([Figures 3J](#), [S3E](#), and [S3F](#)). Immunohistochemical analysis validated regional differences in the expression of *WNT7B* and *NR2F2* and revealed cell-type-specific differences in their expressions. Immunolabeling for *WNT7B* was enriched in future layer 5 pyramidal neurons of the occipitotemporal cortical plate, which were organized into columns ([Figure S4A](#)). *NR2F2* was enriched in the upper part of the fetal temporal cortical plate including the islets in the entorhinal cortex ([Figure S4B](#)).

Adolescence and adulthood coexpression modules exhibited more stability over time and less complex spatial patterns

([Figures 4A–4E](#) and [S2I–S2L](#)). Consistent with our previous finding of dramatic differences in the number of DEX genes among areas in these periods ([Figure 2C](#)), the most common areal coexpression patterns reflected enrichments in MFC (e.g., M215), V1C (e.g., M214), MFC, and ITC (e.g., M239), and differences between the primary sensory-motor areas (e.g., M269) and association areas (e.g., M183). Expression patterns of several intramodular hub genes were validated with qRT-PCR (median  $r = 0.82$ ), such as *GABRQ* in MFC, *TRPC3* in V1C, *VAV3* in primary sensory areas, and *BAIAP3* in all association areas ([Figures 4F–4I](#) and [S3M–S3T](#)). Together, these findings indicate that the transcriptional hourglass pattern reflects differences over time in processes related to the construction and functional specializations of areas.

### Certain Prenatal Expression Patterns Differ between Human and Macaque

To investigate whether some of the observed temporally regulated interareal expression patterns exhibit interprimate divergence, we performed qRT-PCR on the previously selected intramodular hub genes ([Figures 3I–3L](#), [4F–4I](#), and [S3](#)) in homologous regions of human and rhesus macaque neocortices at equivalent ages ([Supplemental Experimental Procedures](#), Note 5). In total, we analyzed all 11 NCX areal samples in 38 human and 21 macaque developing and adult brains ([Supplemental Experimental Procedures](#), Notes 4 and 5, and [Table S1C](#)). Of the hub genes that had prominent interareal differential expression prenatally but not postnatally (*CLMP*, *C13ORF38*, *NR2F2*, *WNT7B*, *KCNK12*, and *WBSR17*), only *NR2F2* and *WNT7B* had spatiotemporal areal expression profiles that were well correlated ( $r > 0.8$ ) between human and macaque, indicating that their expression patterns are well conserved. In contrast,

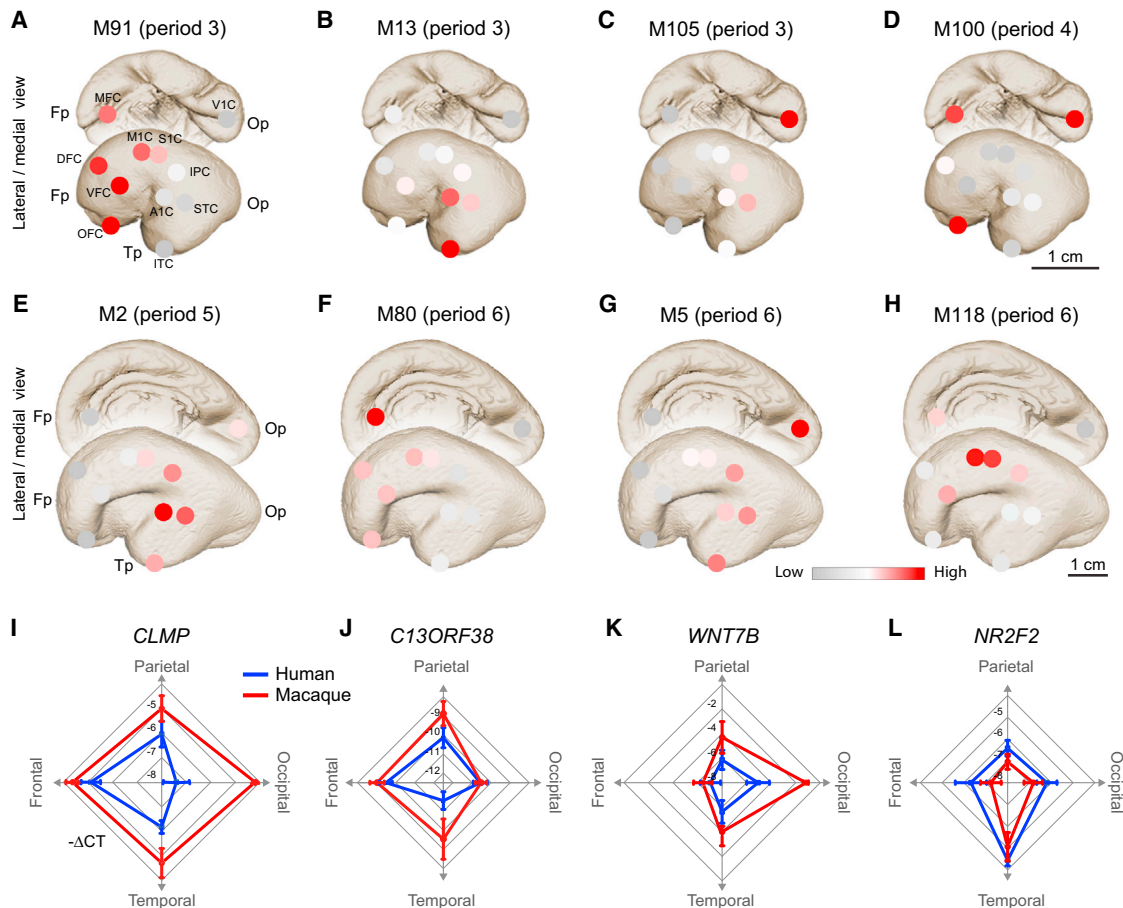


**Figure 3. Fetal Gene Coexpression Modules and Hub Genes in Human and Macaque Monkey**

(A–H) Average scaled expression of all genes in coexpression module (M) 91, M13, M105, M100, M2, M80, M5, and M118 show a gradient-like expression pattern in periods 3 (A–C), 4 (D), 5 (E), and 6 (F–H).

(I–L) Radar charts of qRT-PCR of intramodular hub genes *CLMP* (M91) (I), *C13ORF38* (M80) (J), *WNT7B* (M6) (K), and *NR2F2* (M13) (L) demonstrate a gradient-like expression pattern in human (blue) in directions of areas grouped by their corresponding lobes (e.g., frontal, parietal, occipital, and temporal; versions of these radar charts with all 11 areas across different periods are shown in Figures S3A–S3L). Rhesus macaque (red) expression patterns are similar to those of human. See also Figures S2, S3, and S4 and Table S4.

the interareal expression pattern of *WBSCR17* was only conserved during late-fetal periods ( $r > 0.8$ ), while *KCNK12* had moderate correlation only during early fetal periods ( $r = 0.63$ ), indicating that some of the spatiotemporal expression patterns are shaped by regulatory programs that differ between humans and NHPs (Figures 3I–3L and S3A–S3L). Comparative analysis of adolescent and adult intramodular hub genes (*BAIAP3*, *GABRQ*, *TRPC3*, and *VAV3*) revealed that the interareal expression patterns of *BAIAP3* and *VAV3* were conserved in both adolescent and adult human and macaque NCX ( $r > 0.8$ ) (Figures 4F–4I and S3M–S3T). In contrast, the spatial expression patterns of *GABRQ* and *TRPC3* were only conserved in adulthood ( $r > 0.8$ ) but not in adolescence ( $r \leq 0.6$ ). While limited in their scope, these findings show that certain intramodular hub genes exhibit temporally regulated and species-differential interareal expression patterns and may reflect broader differences in developmental gene expression programs between the two primates.

### Increased Synchronization of Postnatal Areal Transcriptional Trajectories

Previous work has shown that NCX areas mature at different rates with primary sensory-motor areas maturing first, followed by association areas (Flechsig, 1901; Rapoport and Gogtay, 2008; Sowell et al., 2003). To investigate the transcriptional dynamics associated with areal maturation, we generated intra-areal global expression trajectories by correlating the transcriptome profile of each sample to the averaged transcriptome profile of the corresponding area in midadulthood (period 14; Supplemental Experimental Procedures, Note 3.5.1). We also correlated the transcriptome profiles to the corresponding putative area in early fetal development (period 3), to control for putative bias of selecting a specific period (Figure 5A). These trajectories allowed us to detect large-scale changes in the transcriptome over time in individual putative functional areas. Surprisingly, all areal maturational trajectories had similar shapes, with steep increases during mid- and late fetal

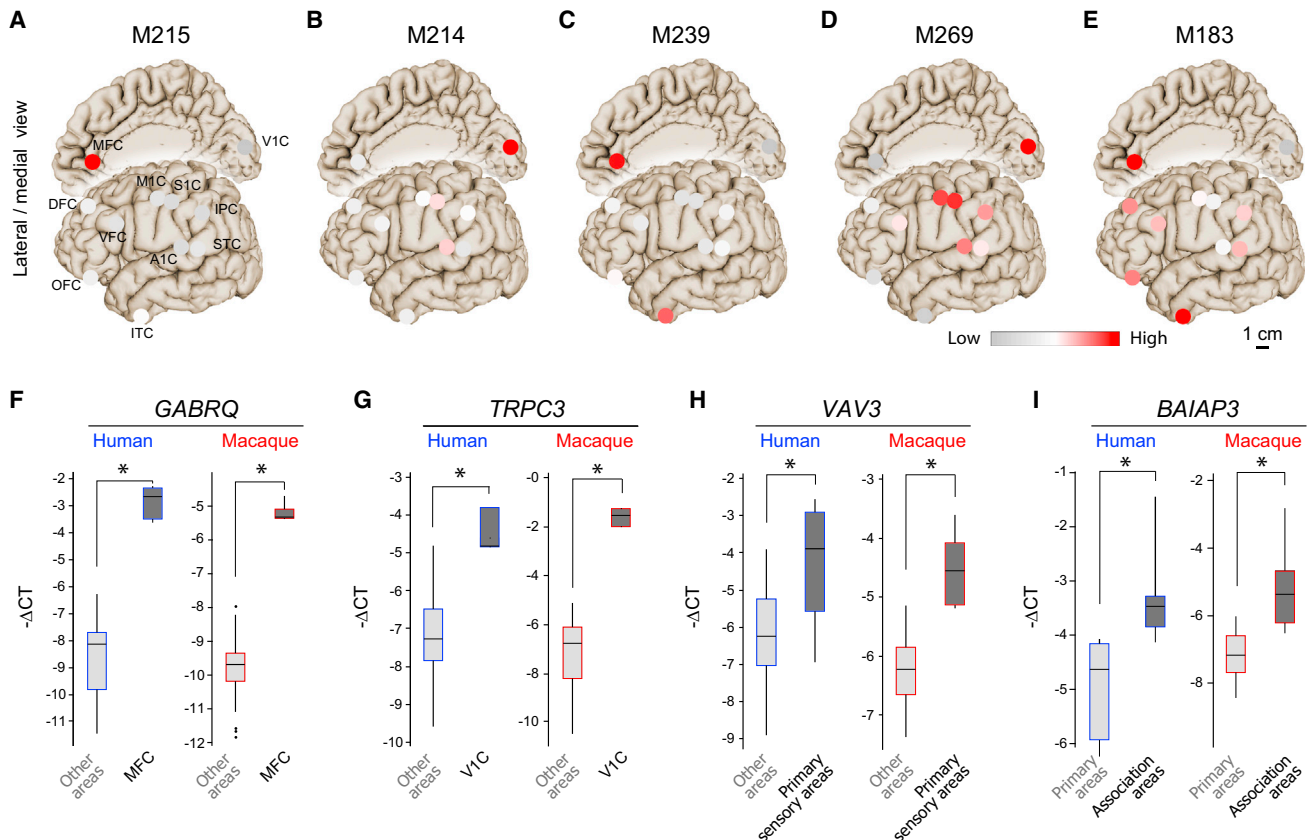


**Figure 4. Adolescent/Adult Gene Coexpression Modules and Hub Genes in Human and Rhesus Macaque**

(A–E) Average scaled-expression of all genes in M215, M214, M239, M269 and M183, in period 13, shows area-specific (A–C) or primary (D) sensory and associative (E) area-specific patterns.

(F–I) Box plots show qRT-PCR expression levels of area-enriched human (blue) and rhesus macaque genes (red): *GABRQ* (M215) (F) and *TRPC3* (M214) (G). Boxes represent the 25<sup>th</sup> and 75<sup>th</sup> percentiles. Whiskers represent the fifth and 95<sup>th</sup> percentiles. Genes with patterns that discriminate primary sensory areas and associative areas are also shown: *VAV3* (M214) (H) and *BAIAP3* (M183) (I), respectively. Radar charts of qRT-PCR data for the four genes with all 11 areas across different periods are shown in Figures S3M–S3T. Error bars represent SD. See also Figures S2 and S3.

development and the major inflection point on the curve during late infancy (Figure 5A). However, the average deviation of the areal trajectory from the average overall maturational trajectory (maturational difference index; see Supplemental Experimental Procedures, Note 3.5.2) varied more among putative areas during fetal than postnatal periods (Figure 5B). MFC and ITC appear to mature faster than other areas prenatally, while DFC and V1C mature slower. Thus, interareal differences in maturational rates did not follow the global anteroposterior or mediolateral neurogenetic gradients observed in rodents (Bayer and Altman, 1987). Furthermore, these findings indicate that at the global level putative areal transcriptomes become more synchronized during postnatal development. Interestingly, we also observed a decline in some areal trajectories, most prominently in V1C, in period 15. Moreover, V1C changes in aging deviate in the same direction in both fetal and adult trajectories, suggesting that the changes are not a reversal toward fetal expression as previously reported (Colantuoni et al., 2011) but instead are likely unique to the aging process. These transcriptome changes could not be explained by the difference in confounding factors

between V1C and non-V1C areas (RIN,  $p = 0.41$ ; PMI,  $p = 1$ ; pH,  $p = 1$ ) or between adult periods (RIN,  $p = 0.96$ ; PMI,  $p = 0.84$ ; pH,  $p = 0.13$ ). Consistent with previous findings in aged prefrontal cortex (Colantuoni et al., 2011), this suggests that aging is associated with global transcriptomic changes that vary considerably among NCX areas.

Next, we followed the maturational trajectories of specific neurobiological processes and categories, using the first principal component to summarize the expression of genes associated with various developmental processes (Supplemental Experimental Procedures, Note 3.6). Notable trajectories and differences in their onset times, rates of increase and decrease, and shapes were observed within and between putative areas. Many showed more prominent interareal variations prenatally than postnatally (Supplemental Experimental Procedures, Note 3.6, and Figures S5 and S6). These included cell proliferation (which displayed anteroposterior and mediolateral gradients), dendrite development, and synapse development (which showed accelerated rate in M1C and S1C). Some trajectories, such as myelination, were variable both prenatally and

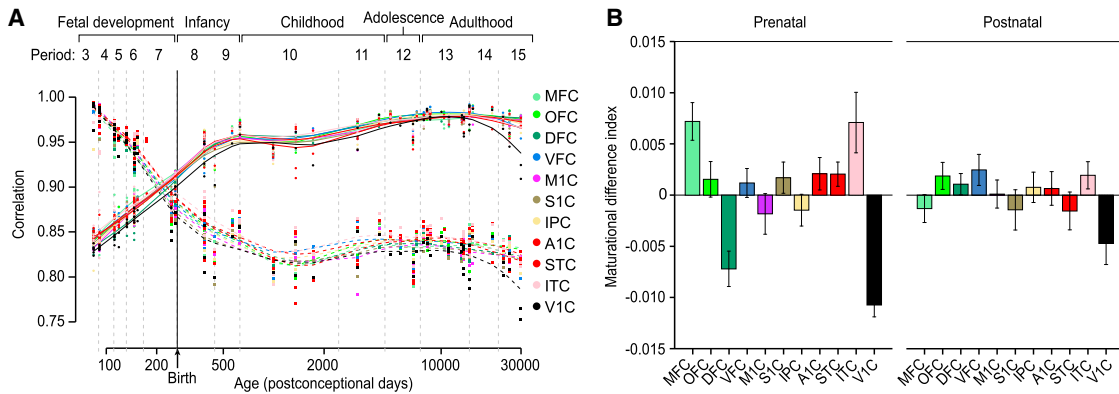


**Figure 5. Areal Transcriptional Trajectories Become More Synchronized during Postnatal Development**

(A) A maturational trajectory plot shows the Pearson correlation of gene expression in each sample to the corresponding averaged gene expression in period 14 (solid line) or period 3 (dashed line).

(B) Bar plots show the average deviation of the areal trajectory from the average overall maturational trajectory (maturational difference index). Prenatal (fetal) development exhibits more deviation than postnatal development. Error bars represent SD. See also Figures S5 and S6.

postnatally (Figures S6E and S6F). These findings indicate that specific transcriptional trajectories, similar to interareal divergence, vary across the putative areas, with prenatal development being generally more variable.

### Putative Areal Transcriptomes Are Globally Symmetric across Time

Since the initial discoveries of the functional lateralization of speech and language in the perisylvian areas of the NCX (Broca, 1861; Dax, 1865; Wernicke, 1874), an abundance of data has demonstrated functional and structural asymmetries between hemispheres (Amunts et al., 2003; Chi et al., 1977; Cullen et al., 2006; Geschwind and Levitsky, 1968; Hayes and Lewis, 1993; Kasprian et al., 2011). However, transcriptome studies of left-right differences in NCX gene expression are rare and limited by a small and temporally restricted data set (Hawrylycz et al., 2012; Johnson et al., 2009; Lambert et al., 2011; Sun et al., 2005). Furthermore, previous findings are also inconsistent, as evidence for gene expression asymmetry has been found in early fetal (Sun et al., 2005), but not in midfetal or adult, NCX (Hawrylycz et al., 2012; Johnson et al., 2009; Lambert et al., 2011). Since gene expression differences between hemispheres might be subtle, we relaxed our criteria and used an FDR < 0.1 without fold change cutoff. Nevertheless, we failed to identify statistically significant interhemispheric differences across fetal and postnatal time span, using a paired t test (Figures 6A and 6B).

Since microarray-based analyses are limited to those genes included in the platform, we further investigated the lateralization of gene expression using mRNA-sequencing (mRNA-seq). This technique allows for unbiased profiling of mRNA transcripts in a wider dynamic range than microarrays (Wang et al., 2009) and thus can detect rare and unknown transcripts as well as more subtle gene expression differences between samples. We performed mRNA-seq (see Figure S7 for quality control measures) on the left and right STC samples from 11 randomly selected brains covering the fetal and postnatal time span (periods 3–15; Table S1B). STC plays an important role in lan-

guage lateralization (Geschwind and Levitsky, 1968; Wernicke, 1874) and is the earliest NCX area known to show signs of structural asymmetry in the fetal brain (Chi et al., 1977; Kasprian et al., 2011). mRNA-seq analysis detected only one gene (*SHANK3*) with a statistically significant (FDR < 0.1) left-right bias in expression (Figure 6C). However, the right-biased *SHANK3* expression was not detected in the larger number of samples analyzed by exon array extended probe sets (data not shown). This indicates that the asymmetric *SHANK3* expression observed with mRNA-seq was probably due to the sampling of a subset of analyzed fetal brains, as this bias disappeared when a larger number of brains were analyzed.

To test the concept of the arrival of corresponding developmental stages sooner in the right than in the left hemisphere (Taylor, 1969; Thatcher et al., 1987), we compared the individual areal maturational trajectories between hemispheres. This analysis revealed no trend in faster maturation of one hemisphere over the other (Figure 7). Our findings indicate that, at the population level, areal transcriptomes are globally symmetric across the full course of human neocortical fetal development and adulthood.

### DISCUSSION

Our analyses of the temporal dynamics and bilaterality of putative areal transcriptomes revealed several unexpected aspects of human neocortical development. We uncovered that the degree of transcriptional differences between areas, as measured by the number of DEX genes, is regulated over time in an hourglass pattern. The greatest interareal differences were found prenatally, followed by a phase of minimal interareal transcriptional divergence during infancy and childhood and the increase in interareal difference, to a slighter degree, from adolescence onward.

We also provided evidence that these three major phases of interareal transcriptional divergence reflect underlying developmental and functional differences. Fetal DEX genes and coexpression modules had highly dynamic spatiotemporal

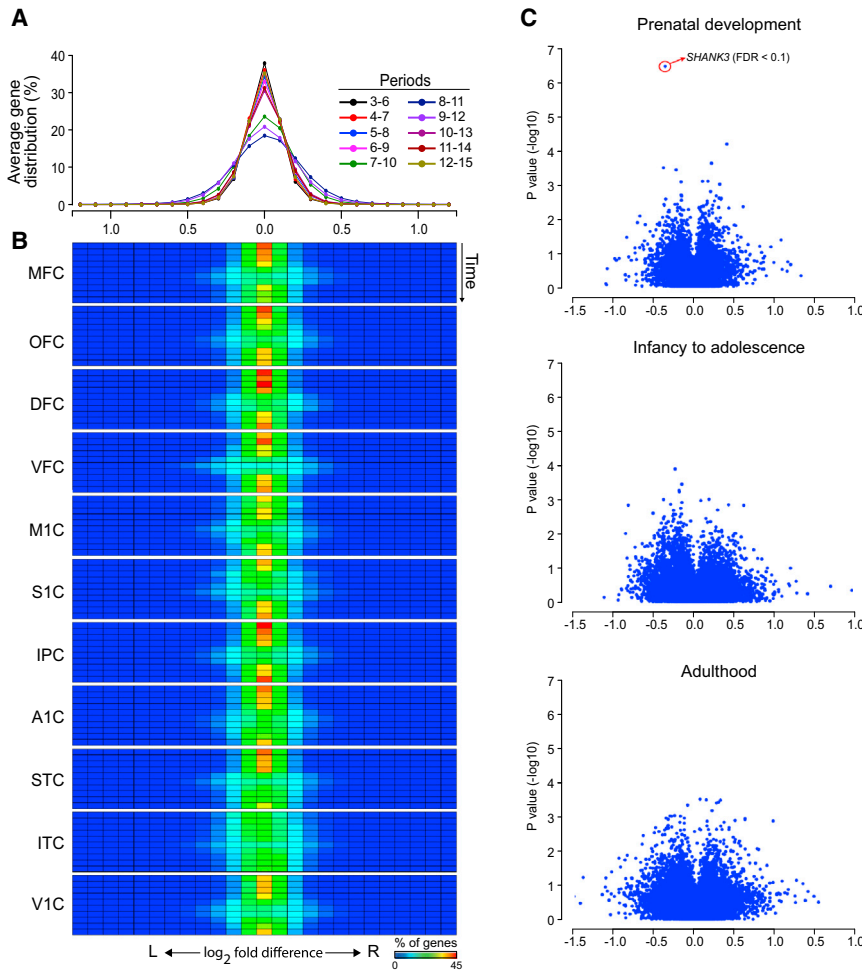


**Figure 6. Areal Transcriptomes Are Globally Symmetric at the Population Level across Fetal Development and Postnatal Lifespan**

(A) Average distribution of hemispheric bias for all profiled neocortical areas through overlapping time points of development and adulthood. (B) A heat map shows the distribution of fold differences in expression of all analyzed genes between left and right hemispheres for each profiled neocortical area across time using the exon array technique. Each row corresponds to a four-period sliding window (first row: 3–6; last row: 12–15). (C) RNA-seq analysis of interhemispheric bias. Volcano plots show the range of fold differences and p values of gene expression between left and right hemispheres in fetal, infancy to adolescence, and adulthood. *SHANK3* is the only significantly DEX gene, during the fetal period (FDR threshold of 0.1), but with low fold ratio. See also Figure S6 and Table S5.

extended period of infancy and childhood, during which time areas become more transcriptionally similar. In addition, the global gene expression maturational trajectories become more synchronized over the course of early postnatal development. We hypothesize that this areal transition from high divergence to similarity as well as increased synchronization are related to coincidental changes in neurodevelopmental processes. Over one hundred years ago, Brodmann discovered (Brodmann, 1909) that the anatomy of the entire neocortical plate is transiently transformed by the appearance of an ontogenetic six-layered Grundtypus (i.e., the fetal equivalent of future layers 2–6) during late fetal and neonatal development (periods 7 and 8 in this study). During those periods layer 5 pyramidal neurons also transiently express nitric oxide synthase 1 protein throughout the human NCX (Kwan et al., 2012). In addition, the human NCX exhibits more widespread synchronized intra- and interhemispheric network activity around birth and in infancy (Fransson et al., 2007; Khazipov and Luhmann, 2006). Thus, these global molecular and functional changes in the late fetal and neonatal human NCX may provide the mechanisms by which areas become more similar in their expression patterns.

expression patterns and tended to be related to early neurodevelopmental processes associated with cell generation and neural circuit construction. Consistent with this finding, previous neuroanatomical studies have shown that area-specific features of axonal projections and neuronal differentiation are already evident in the midfetal NCX (Johnson et al., 2009; Kwan et al., 2012; Vasung et al., 2010). Interestingly, the relative contribution of areas to the overall interareal transcriptional divergence varied across fetal development and may reflect the underlying processes involved in areal patterning. Additionally, our results indicate that fetal MFC and ITC, which have high numbers of DEX genes and global transcriptional trajectories that point to faster maturation, may have differentiated earlier than other analyzed areas. This developmental pattern brings to mind the evolutionary pattern of NCX differentiation arising from dual archicortical and paleocortical moieties (Sanides, 1969). Also, the increased transcriptional divergence of prospective primary motor-sensory areas (V1C, A1C, S1C, and M1C) is suggestive of their early transcriptional specifications.

The fetal phase of robust transcriptional differences is followed by a phase of sharply reduced interareal transcriptional divergence that spans late fetal development through the

appearance of an ontogenetic six-layered Grundtypus (i.e., the fetal equivalent of future layers 2–6) during late fetal and neonatal development (periods 7 and 8 in this study). During those periods layer 5 pyramidal neurons also transiently express nitric oxide synthase 1 protein throughout the human NCX (Kwan et al., 2012). In addition, the human NCX exhibits more widespread synchronized intra- and interhemispheric network activity around birth and in infancy (Fransson et al., 2007; Khazipov and Luhmann, 2006). Thus, these global molecular and functional changes in the late fetal and neonatal human NCX may provide the mechanisms by which areas become more similar in their expression patterns.

The drop in interareal transcriptional divergence extends throughout early postnatal development when neocortical map undergoes reorganization largely through the influence of experience and environmental and social inputs (Johnson, 2001). Furthermore, infancy and childhood are critical and sensitive periods for the acquisition and refinement of cognitive and motor functions characterized by substantial plasticity (Johnson, 2001; Rapoport and Gogtay, 2008). Thus, we hypothesize that after the initial establishment of area-specific subcortical and corticocortical projections during prenatal

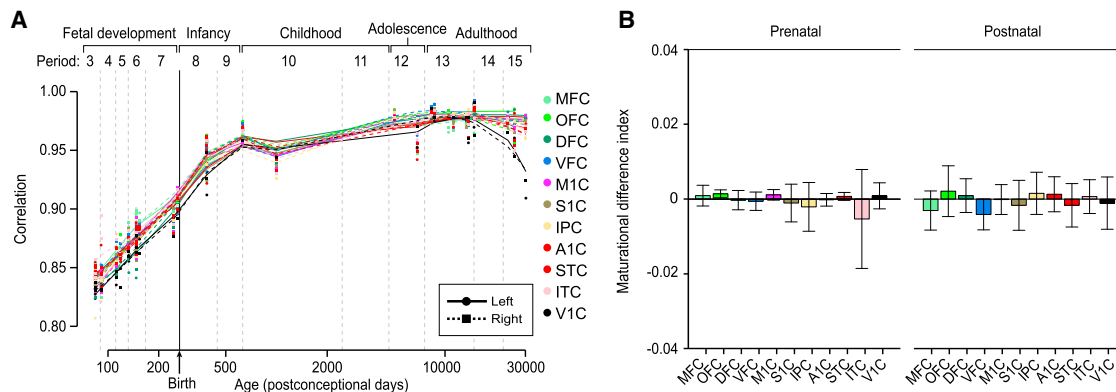


**Figure 7. Population-Level Global Areal Transcriptional Expression Trajectories Are Bilaterally Symmetric**

Transcriptional maturational trajectories of left (solid line) and right (dashed line) hemispheres of each NCX area (A) and maturational difference index between hemispheres in prenatal (fetal) and postnatal development (B) demonstrate a symmetric global gene expression profile. Error bars represent SD.

development, the robust interareal transcriptional differences are no longer needed and are superseded by more general neuronal and glial differentiation transcriptional programs involved in the maturation of neural circuits. Some of these more general programs, such as the transcription of myelination genes, also exhibit interareal difference in the neonatal and postnatal NCX, but they appear to be less robust or less dynamically regulated than many fetal programs. Specific transcriptional trajectories seem to be more synchronized between areas than expected from analyses of maturational trajectories of several phenotypic traits such as synaptogenesis (Huttenlocher and Dabholkar, 1997), cortical thickness (Giedd et al., 1999; Sowell et al., 2003), and myelination (Flechsig, 1901). This observation also suggests that some phenotypic interareal differences arise in part by posttranscriptional and activity-dependent mechanisms. Interestingly, in contrast to the classic hierarchical model of human cortical areal development, the peak of synaptogenesis and overproduction of neurotransmitter receptors occur concurrently among layers and areas of the developing macaque cerebral cortex (Rakic et al., 1986; Lidow et al., 1991).

Interareal transcriptional divergence increases again during adolescence, a period of great developmental changes in the human brain (Giedd et al., 1999; Johnson, 2001; Sowell et al., 2003), and throughout adulthood as the brain matures and ages. Unlike genes from the fetal phase, DEX genes and co-expressed genes during adolescence and adulthood tend to be related to categories such as synaptic transmission and cell-cell signaling. Thus, adolescence and adulthood, especially the aging process, are accompanied by specific changes in regional/areal transcriptomes.

Interestingly, the temporal pattern of interareal transcriptional divergence resembled the hourglass model of transcriptome divergence among various species of fruit fly (Domazet-Lošo and Tautz, 2010; Kalinka et al., 2010). We show here that some of the genes that show interareal differential expression over time also display divergence between humans and rhesus macaques, suggesting a possible role for differences in gene expression patterns in human evolution.

The finding of dramatic temporal differences in interareal patterns of gene expression also points to even small differences in age as an important confound in the analysis of areal differences in gene expression across development in healthy and disease brains.

Our findings also show that putative areal transcriptomes are largely symmetrical at the population level and that left and right hemispheres mature at similar rates across the full course of human fetal development and adulthood. Noteworthy, our study design does not allow us to exclude the possibility that there could be transcriptional asymmetry present in areas we did not profile, that we are overlooking asymmetry diluted at the population level by interindividual variations, that asymmetry might be limited to the small subset of genes not present on the array or uniquely mapped by RNA-seq, or that it might be driven by more subtle changes in specific cellular components that we were unable to detect. Our findings are consistent with structural imaging studies showing strong bilateral symmetry of the neocortex (Chen et al., 2011) as well as reports of an unexpectedly high percentage of monozygotic twin pairs that are discordant for handedness (see McManus and Bryden, 1991). Together, these observations suggest that at least some of the aspects of neocortical asymmetry could be driven by stochastic, hormonal, epigenetic, functional connectivity-based, and/or experience-dependent mechanisms (see also Geschwind and Galaburda, 1985; Hobert et al., 2002; McManus and Bryden, 1991; Sun and Walsh, 2006; Toga and Thompson, 2003) that are not clearly reflected in the population-level hemispheric gene expression differences.

## EXPERIMENTAL PROCEDURES

### Samples and Time Periods

For this study, we used a subset of a previously reported data set (Kang et al., 2011). In that data set, the full course of human brain development and adulthood was divided into 15 periods. Neocortical areas from periods 3 to 15 were analyzed in the current study. Additionally, for validation of selected hub genes, we used homologous areas from rhesus macaque, at equivalent developmental periods (Clancy et al., 2007; <http://www.translatingtime.net/>). The complete list of periods and NCX samples, including corresponding putative

functional areas, analyzed in this study can be found in [Table S2](#) and [Figure 1](#), respectively.

Tissue was collected after obtaining parental or next of kin consent and with approval by the institutional review boards at the Yale School of Medicine and at each institution from which tissue specimens were obtained. Tissue was handled in accordance with ethical guidelines and regulations for the research use of human brain tissue set forth by the National Institutes of Health (<http://bioethics.od.nih.gov/humantissue.html>) and the WMA Declaration of Helsinki (<http://www.wma.net/en/30publications/10policies/b3/index.html>).

#### Differential Expression Analyses

We used ANOVA to identify differentially expressed (DEX) genes in the NCX. *p* values from ANOVA were corrected for multiple comparisons using the Benjamini and Hochberg FDR method (Benjamini and Hochberg, 1995), and a conservative statistical threshold (FDR < 0.01 and minimum fold difference >2 between NCX areas) was used to identify DEX genes. To assess the influence of each area to DEX genes, we used a post hoc Tukey's HSD (honestly significant difference) test.

To control for differences in sample size, we used random subsampling to calculate the number of expressed and DEX genes. Samples were divided into three groups: prenatal, postnatal, and adult. The number of samples randomly chosen was calculated as three-fourths of the lowest number of samples contained within any of the three groups. For 100 trials, this fixed number of samples was randomly drawn from each group and the number of expressed or DEX genes was calculated using the selected subset of samples.

#### Transcriptome Maturation

We calculated the mean gene expression for every neocortical area for periods 14 and 3 as references for adulthood and early fetal development, respectively. Then, we compared each sample to their reference sample using Pearson correlation.

We also calculated the average maturational trajectory for all areas. The deviation from the average maturational trajectory for each area was used to calculate the maturational difference index.

#### Weighted Gene Coexpression Network Analysis

WGCNA package (Langfelder and Horvath, 2008, 2012) was applied to samples from periods 3–6 and periods 12–15. Only genes with log<sub>2</sub>-expression value greater than 6 in any sample and coefficient of variation greater than 0.05 were used for analysis. Each module was summarized by an eigen-gene, which is the first principal component of the scaled module expression. Thus, the module eigengene explained the maximum amount of variation of the module expression levels.

#### Gene Ontology Enrichment Analysis

Functional enrichment was assessed using DAVID Bioinformatics Resources 6.7 (Huang et al., 2009a, 2009b).

#### Analysis of Left-Right Bias in Gene Expression

Differences in gene expression between left and right hemispheres were analyzed by the combination of a sliding window algorithm and a paired *t* test. The sliding-window algorithm was used to detect left/right gene expression differences within a group of sequential periods. The window size was set to span four periods.

Using the Illumina sequencing protocol, we also sequenced STC from both left and right hemispheres of 11 brains. After processing the data (see the [Supplemental Experimental Procedures](#) for more details), a paired *t* test was applied to determine whether the expression level of a given gene in one hemisphere was significantly different from that in the other hemisphere, for fetal, postnatal, and adult individuals.

*p* values from *t* tests were transformed to FDR using the Benjamini and Hochberg method (Benjamini and Hochberg, 1995). For each gene, the fold difference (log<sub>2</sub> transformed) between left and right hemisphere samples in each region was also calculated. An FDR of 0.1 was used as a cutoff to identify genes that are DEX between left and right hemispheres in each window.

#### Quantitative Real-Time PCR

An aliquot of the total RNA that was previously extracted from each brain region was used for secondary validation through real-time PCR analysis. One microgram of total RNA was used for cDNA synthesis using SuperScript III First-strand synthesis Supermix (Invitrogen) and subsequently diluted with nuclease-free water to 1 ng/μl cDNA. Gene-specific high-melting temperature primers for genes of interest were designed using NCBI/Primer-BLAST and expressed sequence information obtained from GenBank (NCBI). PCR reactions were conducted on an ABI 7900 Sequence Detection System (Applied Biosystems) using a hot start SYBR-green-based method (Fast SYBR Green Master Mix, ABI) followed by melt curve analysis to verify specificity of the product. The Ct value (cycle number at threshold) was used to calculate the relative amount of mRNA molecules. The Ct value of each target gene was normalized by subtraction of the Ct value from housekeeping genes to obtain the ΔCt value. The relative gene expression level was shown as  $-\Delta Ct$ . All genes of interest were normalized to the housekeeping gene *RPL32*. For each quantitative real-time PCR experiment, three technical replicates from three brains per stage (except in period 7, where we had 2) were used. Monkey brains used for quantitative real-time PCR experiments are listed in [Table S1C](#).

#### ACCESSION NUMBERS

Exon array and RNA-seq data have been deposited under NCBI BioProjects with accession numbers PRJNA134455 and PRJNA223168, respectively.

#### SUPPLEMENTAL INFORMATION

Supplemental Information includes Supplemental Experimental Procedures, seven figures, and five tables and can be found with this article online at <http://dx.doi.org/10.1016/j.neuron.2013.11.018>.

#### ACKNOWLEDGMENTS

We thank M. Horn for helping with processing macaque tissue, Xuming Xu for help with data analyses, and the members of the Šestan laboratory for valuable comments. Human postmortem tissue was obtained from sources listed in the [Supplemental Information](#). Support for predoctoral fellowships was provided by the Portuguese Foundation for Science and Technology (A.M.M.S.), the Croatian Science Foundation (09.01/414; G.S.), the National Science Foundation (DGE-1122492; K.A.M.), and the China Scholarship Council (Y.Z.). This work was supported by grants from the NIH (MH081896, MH089929, NS051869), the Kavli Foundation, NARSAD, the Foster-Davis Foundation, and by a James S. McDonnell Foundation Scholar Award (N.S.).

Accepted: November 4, 2013

Published: December 26, 2013

#### REFERENCES

- Abrahams, B.S., Tentler, D., Perederiy, J.V., Oldham, M.C., Coppola, G., and Geschwind, D.H. (2007). Genome-wide analyses of human perisylvian cerebral cortical patterning. *Proc. Natl. Acad. Sci. USA* 104, 17849–17854.
- Amunts, K., Schleicher, A., Ditterich, A., and Zilles, K. (2003). Broca's region: cytoarchitectonic asymmetry and developmental changes. *J. Comp. Neurol.* 465, 72–89.
- Bayer, S.A., and Altman, J. (1987). Directions in neurogenetic gradients and patterns of anatomical connections in the telencephalon. *Prog. Neurobiol.* 29, 57–106.
- Benjamini, Y., and Hochberg, Y. (1995). Controlling the false discovery rate - a practical and powerful approach to multiple testing. *J. Roy. Stat. Soc. B Met.* 57, 289–300.
- Braak, H., Braak, E., and Bohl, J. (1993). Staging of Alzheimer-related cortical destruction. *Eur. Neurol.* 33, 403–408.
- Broca, P. (1861). Perte de la parole, ramollissement chronique et destruction partielle du lobe antérieur gauche. *Bull. Soc. Anthropol.* 2, 235–238.

- Brodman, K. (1909). Lokalisationslehre der Großhirnrinde in ihren Prinzipien dargestellt auf Grund des Zellenbaues. (Leipzig: Barth).
- Chen, C.H., Panizzon, M.S., Eyler, L.T., Jernigan, T.L., Thompson, W., Fennema-Notestine, C., Jak, A.J., Neale, M.C., Franz, C.E., Hamza, S., et al. (2011). Genetic influences on cortical regionalization in the human brain. *Neuron* 72, 537–544.
- Chi, J.G., Dooling, E.C., and Gilles, F.H. (1977). Left-right asymmetries of the temporal speech areas of the human fetus. *Arch. Neurol.* 34, 346–348.
- Clancy, B., Kersh, B., Hyde, J., Darlington, R.B., Anand, K.J., and Finlay, B.L. (2007). Web-based method for translating neurodevelopment from laboratory species to humans. *Neuroinformatics* 5, 79–94.
- Colantuoni, C., Lipska, B.K., Ye, T.Z., Hyde, T.M., Tao, R., Leek, J.T., Colantuoni, E.A., Elkahlon, A.G., Herman, M.M., Weinberger, D.R., and Kleinman, J.E. (2011). Temporal dynamics and genetic control of transcription in the human prefrontal cortex. *Nature* 478, 519–523.
- Cullen, T.J., Walker, M.A., Eastwood, S.L., Esiri, M.M., Harrison, P.J., and Crow, T.J. (2006). Anomalies of asymmetry of pyramidal cell density and structure in dorsolateral prefrontal cortex in schizophrenia. *Br. J. Psychiatry* 188, 26–31.
- Dax, M. (1865). Lésions de la moitié gauche de l'encéphale coïncidant avec l'oubli des signes de la pensée: Lu au Congrès méridional tenu à Montpellier en 1836. *Gaz. Hebd. Med. Chir.* 2, 259–262.
- Domazet-Lošo, T., and Tautz, D. (2010). A phylogenetically based transcriptome age index mirrors ontogenetic divergence patterns. *Nature* 468, 815–818.
- Faludi, G., and Mirnic, K. (2011). Synaptic changes in the brain of subjects with schizophrenia. *Int. J. Dev. Neurosci.* 29, 305–309.
- Flechsig, P. (1901). Developmental (myelogenetic) localisation of the cerebral cortex in the human subject. *Lancet* 158, 1027–1030.
- Fransson, P., Skiöld, B., Horsch, S., Nordell, A., Blennow, M., Lagercrantz, H., and Åden, U. (2007). Resting-state networks in the infant brain. *Proc. Natl. Acad. Sci. USA* 104, 15531–15536.
- Gazzaniga, M.S., Bogen, J.E., and Sperry, R.W. (1962). Some functional effects of sectioning the cerebral commissures in man. *Proc. Natl. Acad. Sci. USA* 48, 1765–1769.
- Geschwind, N., and Galaburda, A.M. (1985). Cerebral lateralization. Biological mechanisms, associations, and pathology: III. A hypothesis and a program for research. *Arch. Neurol.* 42, 634–654.
- Geschwind, N., and Levitsky, W. (1968). Human brain: left-right asymmetries in temporal speech region. *Science* 161, 186–187.
- Giedd, J.N., and Rapoport, J.L. (2010). Structural MRI of pediatric brain development: what have we learned and where are we going? *Neuron* 67, 728–734.
- Giedd, J.N., Blumenthal, J., Jeffries, N.O., Castellanos, F.X., Liu, H., Zijdenbos, A., Paus, T., Evans, A.C., and Rapoport, J.L. (1999). Brain development during childhood and adolescence: a longitudinal MRI study. *Nat. Neurosci.* 2, 861–863.
- Harrison-Uy, S.J., and Pleasure, S.J. (2012). Wnt signaling and forebrain development. *Cold Spring Harb. Perspect. Biol.* 4, a008094.
- Hawrylycz, M.J., Lein, E.S., Guillozet-Bongaarts, A.L., Shen, E.H., Ng, L., Miller, J.A., van de Lagemaat, L.N., Smith, K.A., Ebbert, A., Riley, Z.L., et al. (2012). An anatomically comprehensive atlas of the adult human brain transcriptome. *Nature* 489, 391–399.
- Hayes, T.L., and Lewis, D.A. (1993). Hemispheric differences in layer III pyramidal neurons of the anterior language area. *Arch. Neurol.* 50, 501–505.
- Hill, J., Inder, T., Neil, J., Dierker, D., Harwell, J., and Van Essen, D. (2010). Similar patterns of cortical expansion during human development and evolution. *Proc. Natl. Acad. Sci. USA* 107, 13135–13140.
- Hobert, O., Johnston, R.J., Jr., and Chang, S. (2002). Left-right asymmetry in the nervous system: the *Caenorhabditis elegans* model. *Nat. Rev. Neurosci.* 3, 629–640.
- Huang, W., Sherman, B.T., and Lempicki, R.A. (2009a). Bioinformatics enrichment tools: paths toward the comprehensive functional analysis of large gene lists. *Nucleic Acids Res.* 37, 1–13.
- Huang, W., Sherman, B.T., and Lempicki, R.A. (2009b). Systematic and integrative analysis of large gene lists using DAVID bioinformatics resources. *Nat. Protoc.* 4, 44–57.
- Huttenlocher, P.R., and Dabholkar, A.S. (1997). Regional differences in synaptogenesis in human cerebral cortex. *J. Comp. Neurol.* 387, 167–178.
- Ip, B.K., Wappler, I., Peters, H., Lindsay, S., Clowry, G.J., and Bayatti, N. (2010). Investigating gradients of gene expression involved in early human cortical development. *J. Anat.* 217, 300–311.
- Johnson, M.H. (2001). Functional brain development in humans. *Nat. Rev. Neurosci.* 2, 475–483.
- Johnson, M.B., Kawasawa, Y.I., Mason, C.E., Krsnik, Z., Coppola, G., Bogdanović, D., Geschwind, D.H., Mane, S.M., State, M.W., and Sestan, N. (2009). Functional and evolutionary insights into human brain development through global transcriptome analysis. *Neuron* 62, 494–509.
- Judaš, M., Sedmak, G., and Kostović, I. (2013). The significance of the subplate for evolution and developmental plasticity of the human brain. *Front. Hum. Neurosci.* 7, 423.
- Kaas, J.H. (2012). The evolution of neocortex in primates. *Prog. Brain Res.* 195, 91–102.
- Kalinka, A.T., Varga, K.M., Gerrard, D.T., Preibisch, S., Corcoran, D.L., Jarrells, J., Ohler, U., Bergman, C.M., and Tomancak, P. (2010). Gene expression divergence recapitulates the developmental hourglass model. *Nature* 468, 811–814.
- Kang, H.J., Kawasawa, Y.I., Cheng, F., Zhu, Y., Xu, X., Li, M., Sousa, A.M., Pletikos, M., Meyer, K.A., Sedmak, G., et al. (2011). Spatio-temporal transcriptome of the human brain. *Nature* 478, 483–489.
- Kasprian, G., Langs, G., Brugger, P.C., Bittner, M., Weber, M., Arantes, M., and Prayer, D. (2011). The prenatal origin of hemispheric asymmetry: an in utero neuroimaging study. *Cereb. Cortex* 21, 1076–1083.
- Kennedy, H., and Dehay, C. (2012). Self-organization and interareal networks in the primate cortex. *Prog. Brain Res.* 195, 341–360.
- Khazipov, R., and Luhmann, H.J. (2006). Early patterns of electrical activity in the developing cerebral cortex of humans and rodents. *Trends Neurosci.* 29, 414–418.
- Kwan, K.Y., Lam, M.M., Johnson, M.B., Dube, U., Shim, S., Rašin, M.R., Sousa, A.M., Fertuzinhos, S., Chen, J.G., Arellano, J.I., et al. (2012). Species-dependent posttranscriptional regulation of NOS1 by FMRP in the developing cerebral cortex. *Cell* 149, 899–911.
- Lambert, N., Lambot, M.A., Bilheu, A., Albert, V., Englert, Y., Libert, F., Noel, J.C., Sotiriou, C., Holloway, A.K., Pollard, K.S., et al. (2011). Genes expressed in specific areas of the human fetal cerebral cortex display distinct patterns of evolution. *PLoS ONE* 6, e17753.
- Langfelder, P., and Horvath, S. (2008). WGCNA: an R package for weighted correlation network analysis. *BMC Bioinformatics* 9, 559.
- Langfelder, P., and Horvath, S. (2012). Fast R functions for robust correlations and hierarchical clustering. *J. Stat. Softw.* 46, 1–17.
- Lidow, M.S., Goldman-Rakic, P.S., and Rakic, P. (1991). Synchronized overproduction of neurotransmitter receptors in diverse regions of the primate cerebral cortex. *Proc. Natl. Acad. Sci. USA* 88, 10218–10221.
- Lui, J.H., Hansen, D.V., and Kriegstein, A.R. (2011). Development and evolution of the human neocortex. *Cell* 146, 18–36.
- McManus, I.C., and Bryden, M.P. (1991). Geschwind's theory of cerebral lateralization: developing a formal, causal model. *Psychol. Bull.* 110, 237–253.
- Molnár, Z., and Clowry, G. (2012). Cerebral cortical development in rodents and primates. *Prog. Brain Res.* 195, 45–70.
- O'Leary, D.D., and Sahara, S. (2008). Genetic regulation of arealization of the neocortex. *Curr. Opin. Neurobiol.* 18, 90–100.
- Piao, X.H., Hill, R.S., Bodell, A., Chang, B.S., Basel-Vanagaite, L., Straussberg, R., Dobyns, W.B., Qasrawi, B., Winter, R.M., Innes, A.M., et al. (2004). G

- protein-coupled receptor-dependent development of human frontal cortex. *Science* 303, 2033–2036.
- Preuss, T.M. (2011). The human brain: rewired and running hot. *Ann. N Y Acad. Sci.* 1225 (Suppl 1), E182–E191.
- Rakic, P. (1988). Specification of cerebral cortical areas. *Science* 241, 170–176.
- Rakic, P., Bourgeois, J.P., Eckenhoff, M.F., Zecevic, N., and Goldman-Rakic, P.S. (1986). Concurrent overproduction of synapses in diverse regions of the primate cerebral cortex. *Science* 232, 232–235.
- Rapoport, J.L., and Gogtay, N. (2008). Brain neuroplasticity in healthy, hyperactive and psychotic children: insights from neuroimaging. *Neuropsychopharmacology* 33, 181–197.
- Rash, B.G., and Grove, E.A. (2006). Area and layer patterning in the developing cerebral cortex. *Curr. Opin. Neurobiol.* 16, 25–34.
- Sanides, F. (1969). Comparative architectonics of the neocortex of mammals and their evolutionary interpretation. *Ann. N Y Acad. Sci.* 167, 404–423.
- Sowell, E.R., Peterson, B.S., Thompson, P.M., Welcome, S.E., Henkenius, A.L., and Toga, A.W. (2003). Mapping cortical change across the human life span. *Nat. Neurosci.* 6, 309–315.
- Sun, T., and Walsh, C.A. (2006). Molecular approaches to brain asymmetry and handedness. *Nat. Rev. Neurosci.* 7, 655–662.
- Sun, T., Patoine, C., Abu-Khalil, A., Visvader, J., Sum, E., Cherry, T.J., Orkin, S.H., Geschwind, D.H., and Walsh, C.A. (2005). Early asymmetry of gene transcription in embryonic human left and right cerebral cortex. *Science* 308, 1794–1798.
- Sur, M., and Rubenstein, J.L. (2005). Patterning and plasticity of the cerebral cortex. *Science* 310, 805–810.
- Taylor, D.C. (1969). Differential rates of cerebral maturation between sexes and between hemispheres. Evidence from epilepsy. *Lancet* 2, 140–142.
- Thatcher, R.W., Walker, R.A., and Giudice, S. (1987). Human cerebral hemispheres develop at different rates and ages. *Science* 236, 1110–1113.
- Toga, A.W., and Thompson, P.M. (2003). Mapping brain asymmetry. *Nat. Rev. Neurosci.* 4, 37–48.
- Tripodi, M., Filosa, A., Armentano, M., and Studer, M. (2004). The COUP-TF nuclear receptors regulate cell migration in the mammalian basal forebrain. *Development* 131, 6119–6129.
- Vasung, L., Huang, H., Jovanov-Milošević, N., Pletikos, M., Mori, S., and Kostović, I. (2010). Development of axonal pathways in the human fetal fronto-limbic brain: histochemical characterization and diffusion tensor imaging. *J. Anat.* 217, 400–417.
- Wang, Z., Gerstein, M., and Snyder, M. (2009). RNA-Seq: a revolutionary tool for transcriptomics. *Nat. Rev. Genet.* 10, 57–63.
- Wernicke, C. (1874). *Der Aphasische Symptomenkomplex: Eine Psychologische Studie auf Anatomischer Basis.* (Breslau: Max Cohn & Weigert).

**Neuron, Volume 81**

**Supplemental Information**

**Temporal Specification and Bilaterality  
of Human Neocortical Topographic Gene Expression**

**Mihovil Pletikos, André M.M. Sousa, Goran Sedmak, Kyle A. Meyer, Ying Zhu, Feng  
Cheng, Mingfeng Li, Yuka Imamura Kawasawa, and Nenad Šestan**

# Supplemental Data

## 1. Supplemental Figures

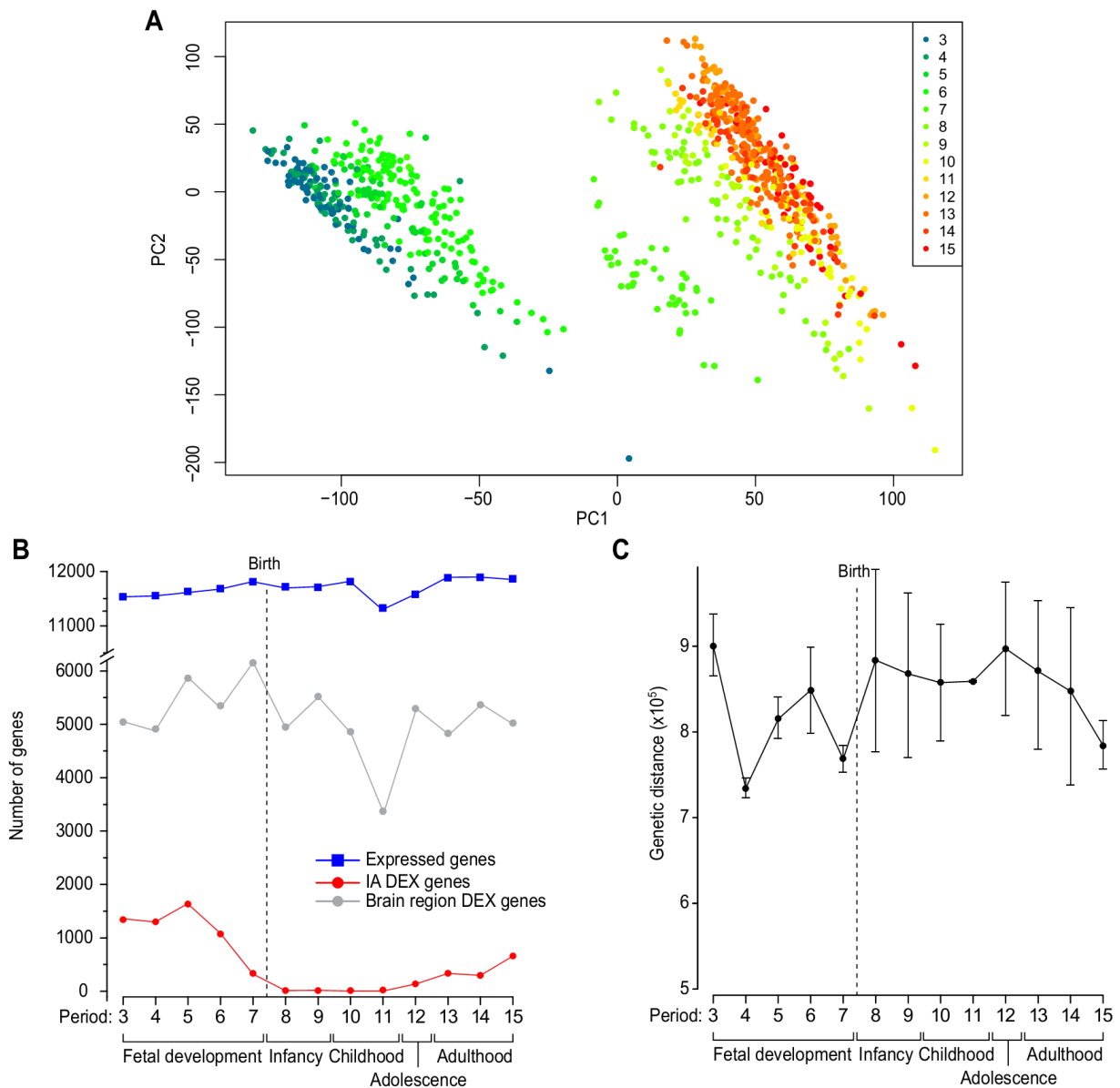


**Figure S1 (associated with Figure 2): Principle component analysis of the NCX samples, number of expressed and inter-areal (IA) DEX genes, and genetic distance among individuals per period**

(A) Principle component analysis, with samples colored by period, shows separation in three distinct clusters: early fetal to late mid-fetal (periods 3-6), late fetal (period 7) and postnatal (periods 8-15). (B) Analysis of neocortical DEX genes (red line) per period shows the hourglass shaped pattern, with the highest number of DEX genes during prenatal period, a lower number of DEX during infancy and childhood, and a reappearance of DEX from adolescence on. The analysis of brain region DEX genes (grey line), which includes neocortex, striatum, cerebellar cortex, hippocampus, mediodorsal nucleus of the thalamus, and amygdala, does not show the hourglass pattern. Number of expressed genes (blue line) stays stable throughout the fetal development and postnatal lifespan. (C) The genetic distance was calculated for each pair of individuals as the number of mismatched alleles detected by Illumina HumanOmni 2.5 SNP arrays. Average distance for each stage was calculated by averaging distance of all possible pairs in the stage. Error bars represent standard deviation.

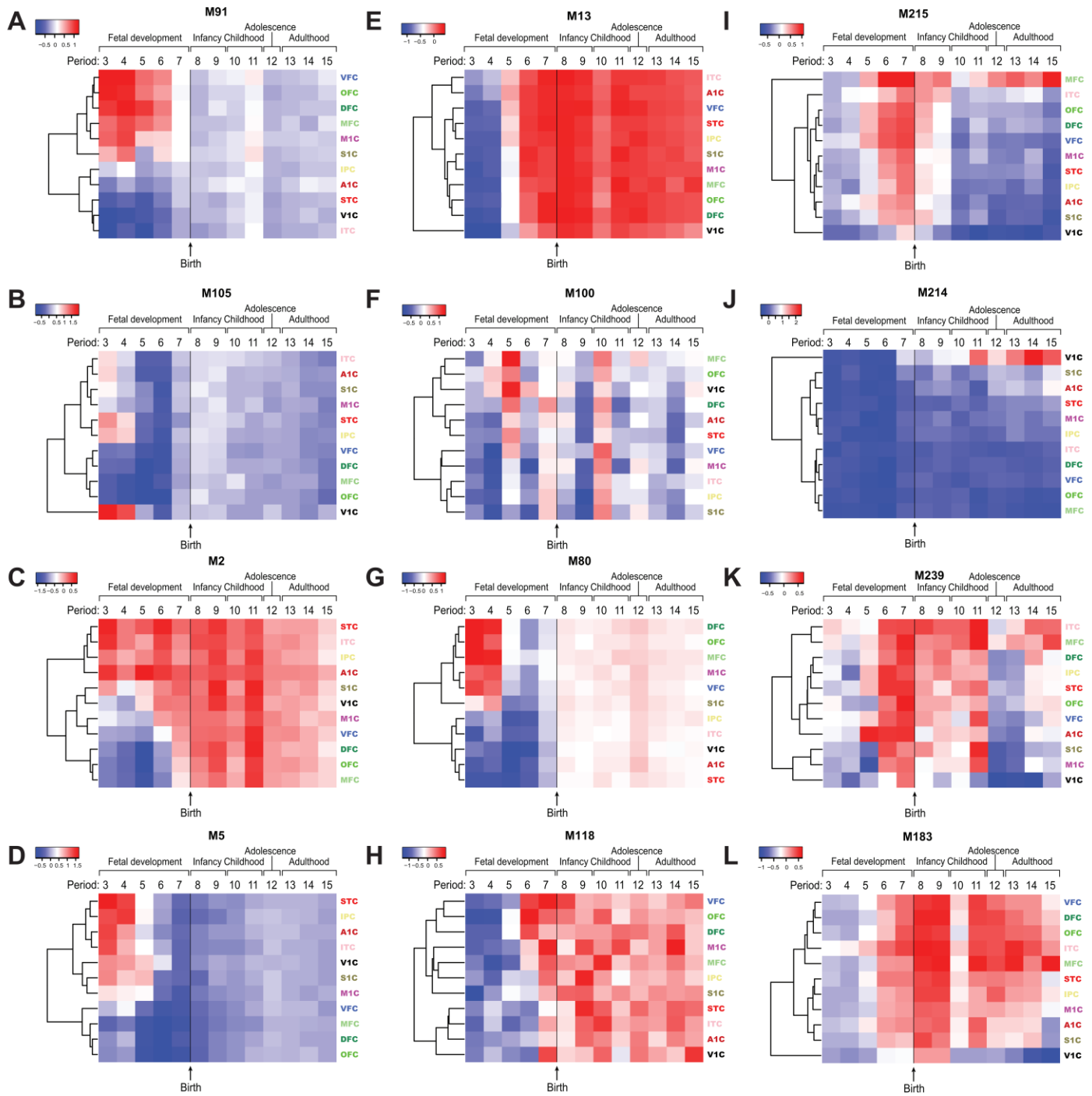


**Figure S2 (associated with Figures 3 and 4): Select WGCNA modules**

(A-H) represent select fetal modules and (I-L) represent adolescent and adult modules.

(A) Heat map showing module 91 (M91) with a frontal-cortex enriched gradient in periods 3-6 (top hub genes: *CYP26A1, HSPA12A, CNIH3, C8orf34, PDE4D, MANBA, ASAM, TSEN15, DPP7, and HS6ST3*); (B) M105 contains genes with expression enriched in occipito-temporal areas in periods 3 and 4 (top hub genes: *SHISA6, KCNK12, DOCK10, PCK2, TMPRSS13, MAS1, STK10, and PPARG*); (C) M2 genes are enriched with posterior perisylvian and temporal expression levels in periods 3-5 (top hub genes: *PCDH9, CAMK4, OSTN, NCAM2, MDGA2, PLEKHH2, and COX7A1*); (D) M5 genes exhibit co-expression patterns in temporo-

parieto-occipital areas in periods 3-5 (top hub genes: *STARD13*, *PAPPA2*, *VRK2*, *SORCS1*, *NXPH3*, *KLHL32*, *CABP7*, *WNT7B*, *OCA2*, and *GPR126*); (E) M13 shows a temporal lobe enriched gradient in period 5 (top hub genes: *LRRC4C*, *GABRB1*, *SLC24A3*, *KLHL4*, *SLC2A13*, *RIT2*, *GRM7*, *CSPG5*, *SV2B*, and *GDA*); (F) M100 genes exhibit expression with a medio-lateral gradient in periods 4 and 5 (top hub genes: *APPL2*, *CTDSP2*, *HDAC1*, *ZNF43*, *NECAP2*, and *HEATR5A*); (G) M80 genes exhibit expression with frontally enriched expression levels (top hub genes: *YPEL2*, *DPF3*, *ZNF385A*, *GADL1*, *SLIT3*, *C13orf38*, *GNG7*, *TCERG1L*, *RCAN3*, and *FAM5B*); (H) M118 genes exhibit expression highest in frontal areas in period 6 (top hub genes: *GDF10*, *ACHE*, *CYB561*, *PDE4A*, *ADAMTS8*, and *TMEM151A*); (I) Heat map of M215 shows genes enriched postnatally in MFC (top genes: *GABRQ*, *SLN*, *CCBE1*, *SCN9A*, *C2orf85*, *ARHGAP6*, *CCDC109B*, *GRID2*, *SYT10*, and *HTR7*); (J) M214 genes are enriched postnatally in V1C (top genes: *TRPC3*, *ITGA11*, *KCNAB3*, *VAV3*, *SYT6*, *DPP4*, *EYA4*, *PTGS1*, *EEPD1*, and *SH3RF2*); (K) M239 genes are enriched in MFC and ITC (top genes: *ADAMTS19*, *CCDC148*, *DPYD*, *GHR*, *ARMC2*, *C2orf60*, *ANKRD7*, *KLHL1*, *COCH*, and *PPM1M*); (L) M183 genes are enriched in associative areas (top genes: *ANO3*, *PRKCG*, *SLIT1*, *SCN3B*, *RAB27B*, *FAM65B*, *SYT17*, *PRKCD*, *PCDH20*, and *PPP4R4*).

Frontal areas: MFC, OFC, DFC, VFC, M1C  
 Parietal areas: S1C, IPC  
 Temporal areas: A1C, STC, ITC  
 Occipital areas: V1C

—■— Human  
 —●— Macaque

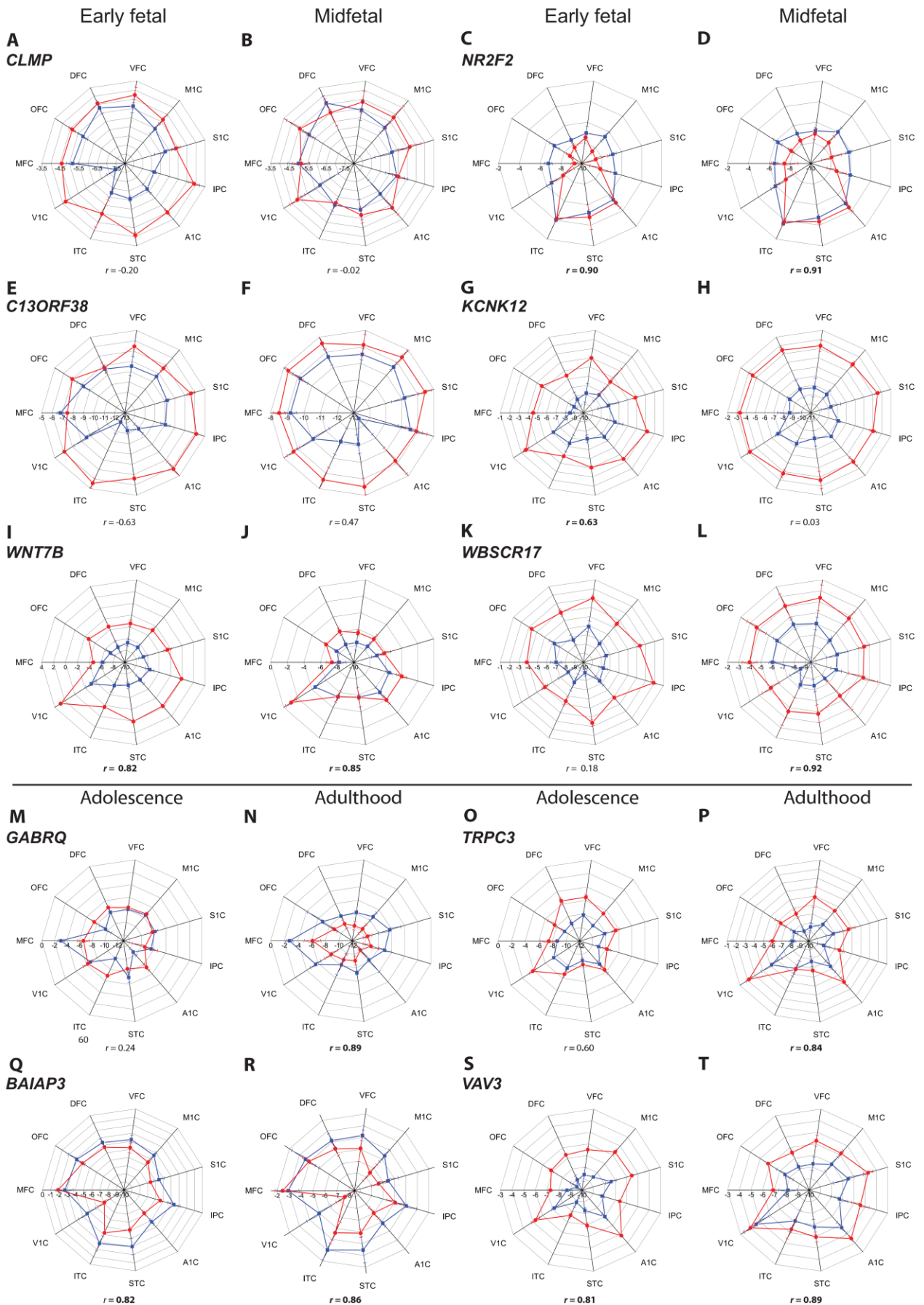


**Figure S3 (associated with Figures 3 and 4): Select qRT-PCR validation**

(A-L) Radar charts showing expression levels ( $-\Delta\text{CT}$ ) in all areas in prenatal periods 3-4 (early) and 5-6 (mid). Pearson's correlation coefficient  $r$  is printed bold when there is positive correlation between human and monkey patterns of expression. The expression pattern is shown with lines and points in blue color for humans and red color for macaque. (A) and (B) *CLMP* shows a different pattern of expression in human and in macaque telencephalon. In human cortex, *CLMP* shows a fronto-occipital gradient during early fetal periods (A), which disappears in midfetal periods (B). (C) and (D) *NR2F2* shows a temporal gradient in both species and in all prenatal periods. (E) and (F) *C13orf38* shows a fronto-temporal gradient in human NCX in both (E) early and (F) midfetal periods, while in macaque NCX the fronto-temporal gradient is not existent; moreover, it is anti-correlated in the early fetal period (E). (G) and (H) *KCNK12* shows an occipito-frontal gradient in both periods in humans, while in macaque it is only during the early fetal period. (I) and (J) *WNT7B* shows the same gradient in human and monkey brains and in both early and mid-fetal periods. (K) and (L) *WBSCR17* shows a correlated fronto-occipital gradient in both species during mid-fetal periods, which is not evident during the earlier periods. Error bars represent standard deviation.

(M-T) Radar charts show the expression levels ( $-\Delta\text{CT}$ ) in all areas in adolescent and adult human and monkey brains. (M) and (N) *GABRQ* exhibits enrichment in MFC in both adolescence and adulthood in human, but only in adulthood of the monkey. (O) and (P) *TRPC3* shows enrichment in V1C in both adolescence and adulthood. (Q) and (R) *BAIAP3* shows enrichment in associative areas, and (S) and (T) *VAV3* shows enrichment in primary sensory areas. Pearson's correlation coefficient  $r$  is printed bold when there is positive correlation between human and monkey pattern of expression. Human expression pattern is shown with blue lines and points while red is used for macaque. Error bars represent standard deviation.

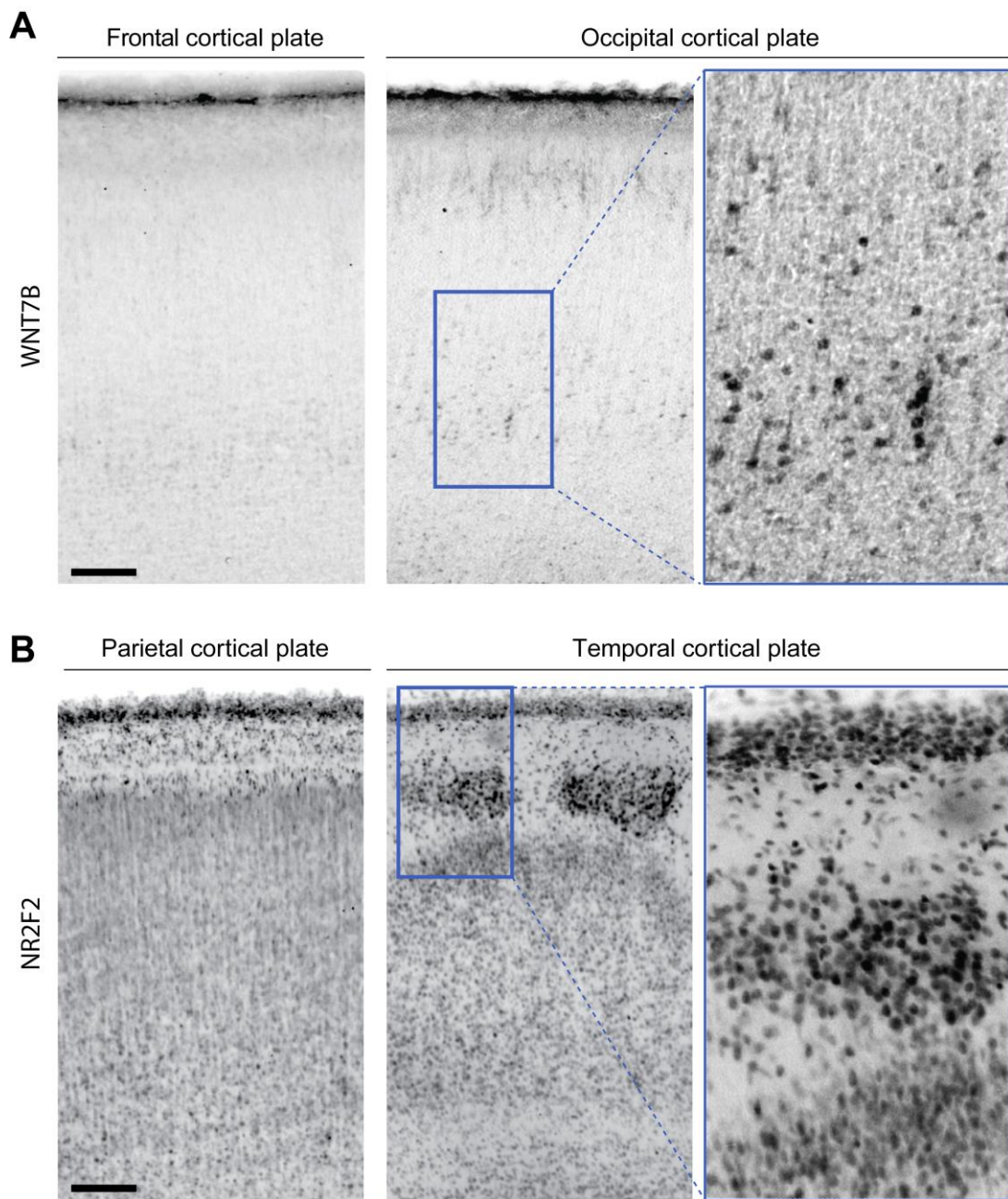


**Figure S4 (associated with Figure 3): Immunohistochemical detection of WNT7B and NR2F2 in the human fetal neocortex at 22 PCW**

(A) Immunohistochemical detection using  $\alpha$ -WNT7B antibody shows lower intensity in frontal cortical plate (left panel) in future layer 5 pyramidal neurons; in the occipital cortical plate (middle panel), the intensity of staining is stronger and there are stained neurons in both layer 3 and layer 5; WNT7B-positive neurons are organized into columns in layer 5 (right panel). (B) Immunohistochemical detection using  $\alpha$ -NR2F2 antibody shows that even though NR2F2 is expressed in the all the analyzed areas, it is clearly more expressed in the inferior temporal cortical plate (middle panel) than in the parietal cortical plate (left panel), corroborating the enrichment in the temporal cortical plate described in Figure 3. Interestingly, NR2F2 shows more immunopositive cells in islets of entorhinal cortical plate (middle panel and right panel detail). Scale bar represents 100  $\mu$ m.

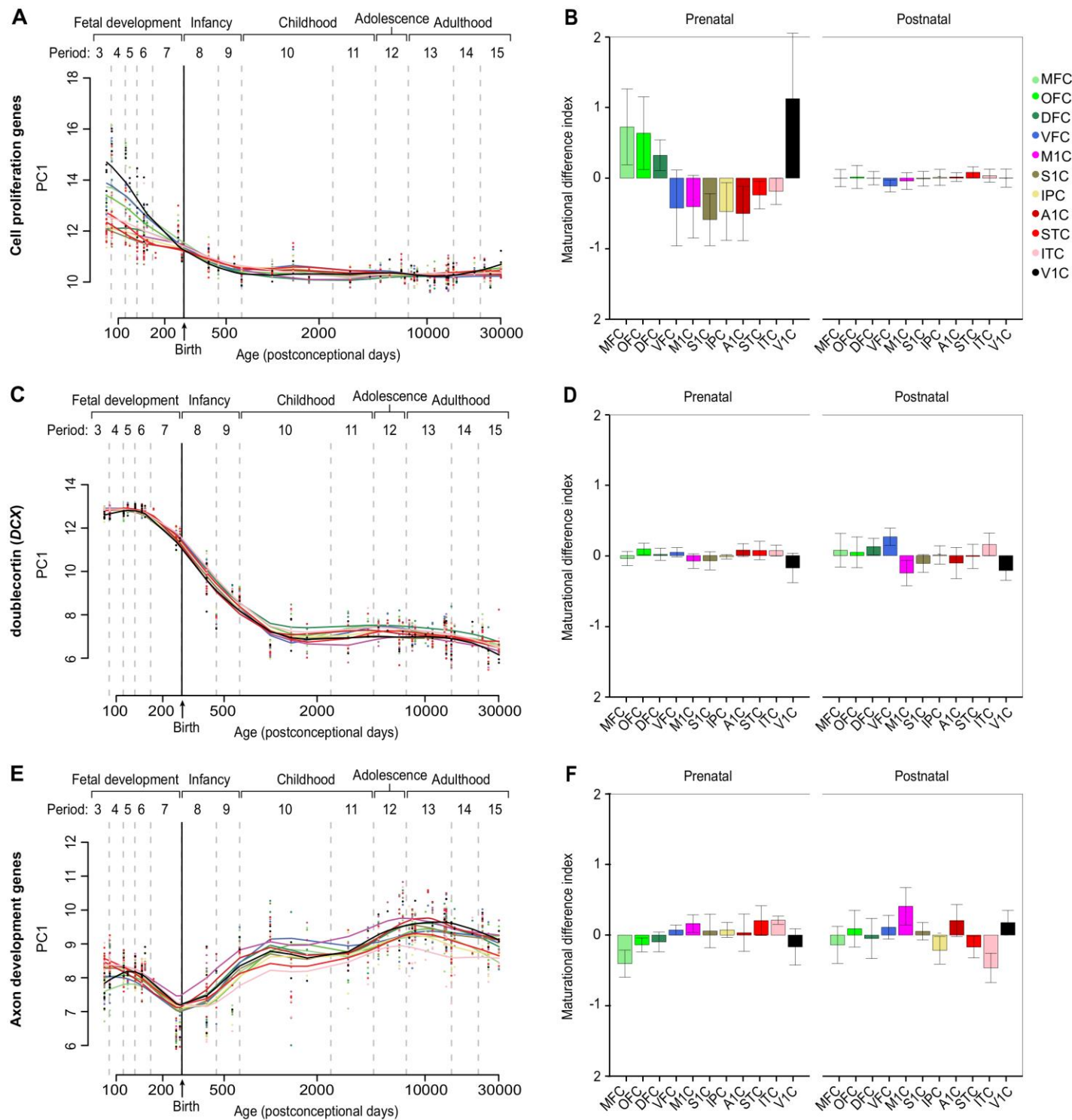


**Figure S5 (associated with Figure 5): Trajectories of genes associated with neurodevelopmental processes**

(A) and (B) Genes associated with cell proliferation markers (*RRM1*, *HES1*, *NES*, and *MKI67*) show higher expression levels and higher variability during prenatal periods than after the birth. (C) and (D) *Doublecortin* (*DCX*), a gene previously associated with neuronal migration and immature neuronal states, shows high expression values during prenatal periods and a big decrease in expression levels during postnatal periods with little deviation from average trajectory. (E) and (F) Axon development marker (*CNTN2*) shows a triphasic trajectory with higher expression during early and mid-fetal and postnatal periods but with decrease in

expression levels around the birth. Deviation from average trajectory is present but relatively low in both prenatal and postnatal periods. Error bars represent standard deviation.

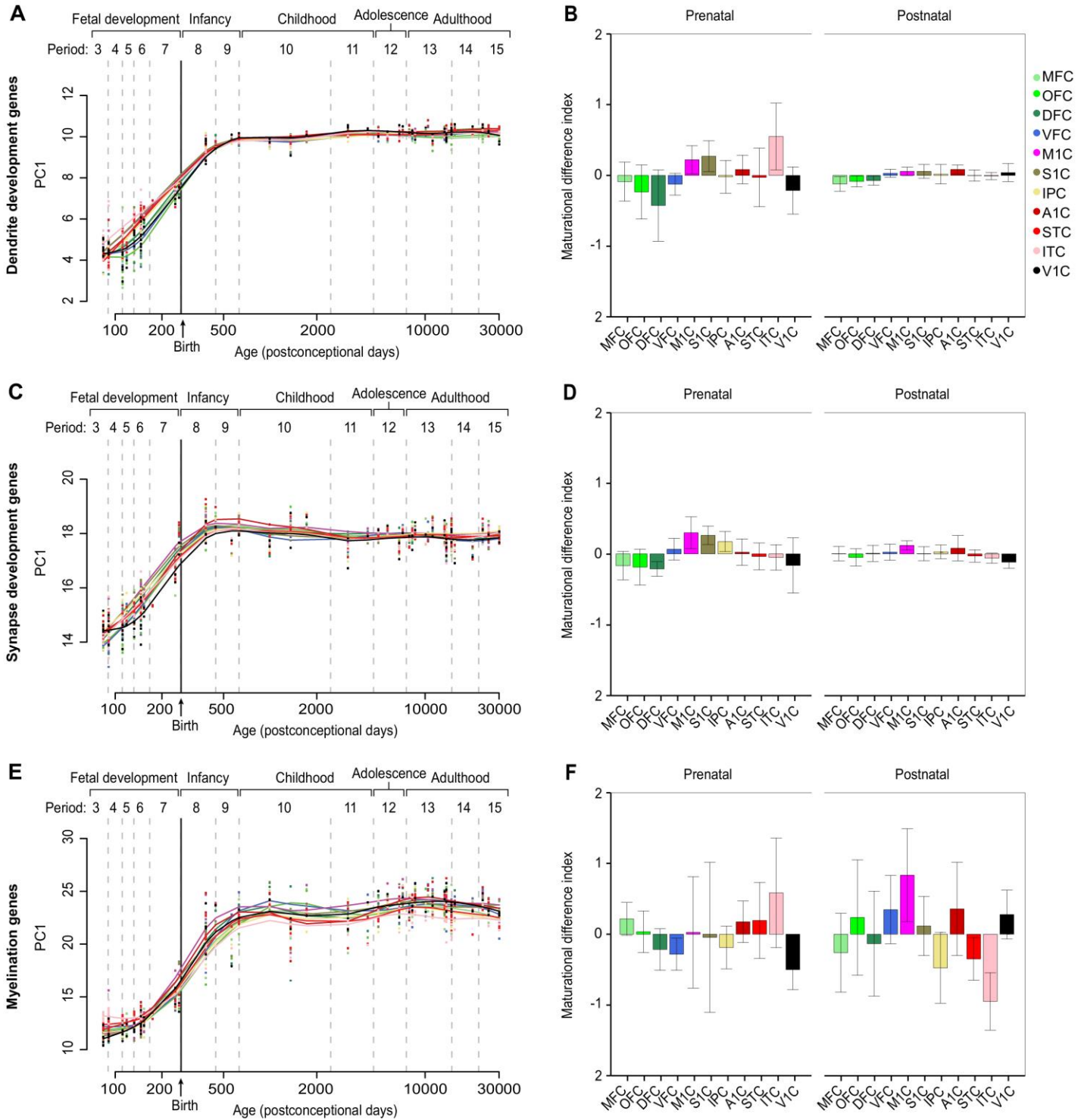


**Figure S6 (associated with Figure 5): Trajectories of genes associated with neurodevelopmental processes**

(A) and (B) Dendrite development genes (*MAP1A*, *MAPT*, and *CAMK2A*) show gradual increases in expression until they reach a plateau at period 10. At prenatal periods, areas show higher deviation from average trajectory than postnatal periods. (C) and (D) Synapse development markers (*SYP*, *SYPL1*, *SYPL2*, and *SYN1*) show increased expression until postnatal periods when they reach a plateau. Deviation from the average trajectory, while present during prenatal periods, virtually disappears after birth. (E) and (F) Myelination genes (*MBP*, *PLP1*, *MOG*, *C11orf9*, and *MAG*) show similar trajectories to the previous two

processes with a steady increase during prenatal periods and reaching a plateau in period 10, but deviation from the average trajectory is present in both prenatal periods. Error bars represent standard deviation.

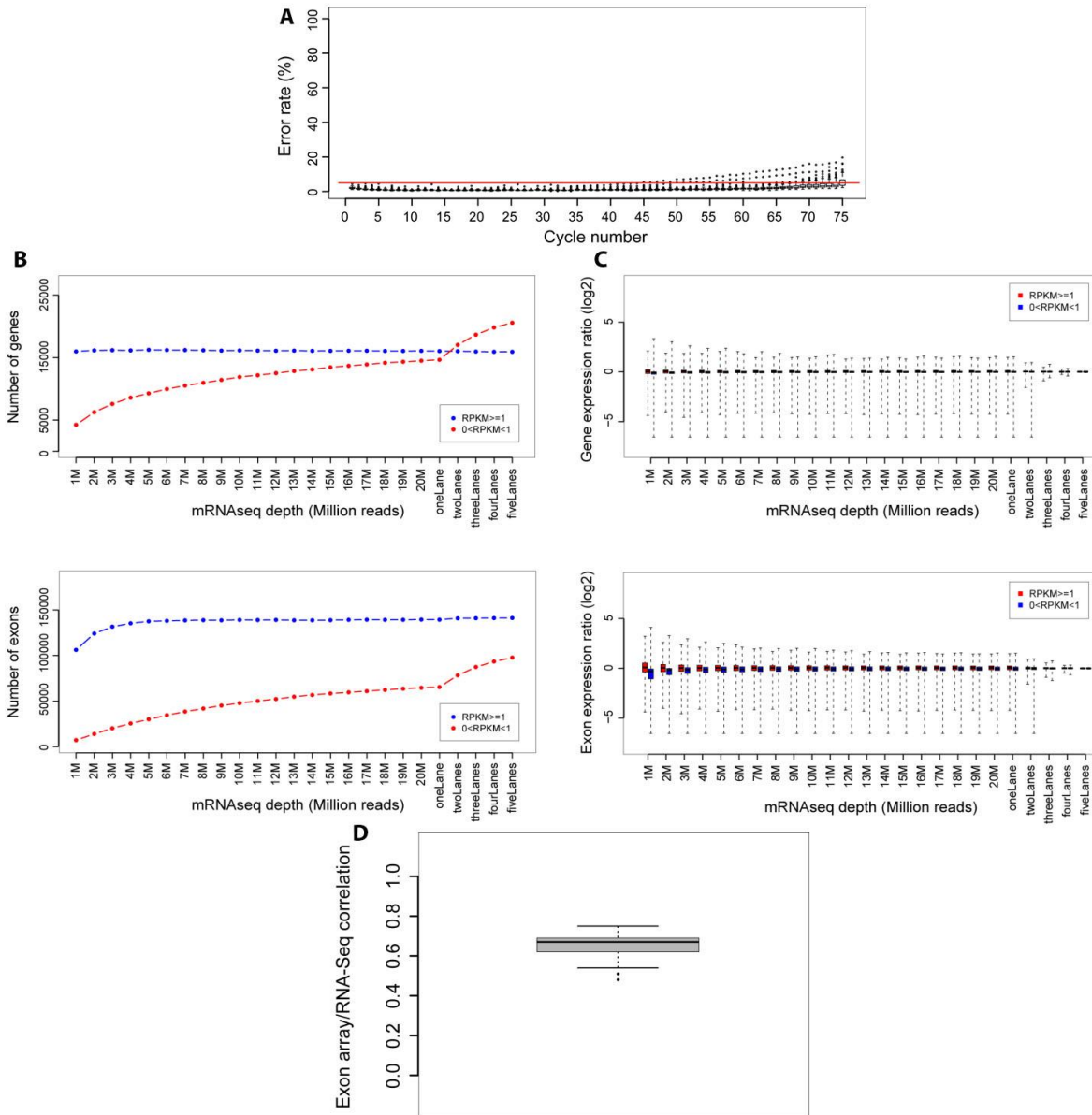


**Figure S7 (Associated with Figure 6): RNA-seq quality control**

(A) Sequencing error rate as a function of cycle number. The sequencing error rate was estimated by the ratio of the alignment mismatch of the sequenced spike-in reads from the reference spike-in RNAs. The distribution of the error rates in each sequencing cycle is shown by box plots, and also ordered by increasing cycle number. The red line represents the 5% limited baseline of error rate. All box plots are under the baseline except a small number of outliers at the end of the number of cycles (75 cycles). The transcriptome survey was evaluated by (B) gene/exon discovery rate and (C) expression variation. The genes and exons were classed into high expressors (RPKM  $\geq 1$ ) and low expressors ( $0 < \text{RPKM} < 1$ ). (B) Discovery rates were a function of sequencing depth. Flat lines indicated that the discovery rate of highly expressed genes (top) and exons (bottom) was less affected by mRNA sequencing depth. The increasing slope of the lines indicated that the low expressing genes (top) and exons (bottom) were more affected by mRNA sequencing depth. (C) Ratios of gene expression and exon expression relative to the combined five technical replicates are shown with box plots and ordered as the simulated sequencing depth. The small variation starting from 10M sampling reads suggested that 10M is the limited baseline for sequencing depth control, although more reads resulted in

improved coverage. **(D)** Correlation between Exon Array and RNA-seq. The Pearson correlation coefficients of their gene expression between the two platforms were shown by box plots. The median value is more than 0.6, suggesting high correlation and comparable equality of transcriptome data obtained from both platforms.

## 2. Supplemental Tables

Supplemental Tables are provided in a single Microsoft Excel file.

### **Table S1 (associated with Figure 1): List of human and macaque brains analyzed in this study**

The brains are ordered by age.

The age of the subject and count for mappable RNA-seq reads are represented for each left and right hemisphere (Table S1B).

### **Table S2 (associated with Figure 1): Periods of human brain development as defined in this study**

List of the periods of human brain development used in this analysis and their corresponding age.

### **Table S3 (associated with Figure 2): Gene Ontology of DEX genes**

List of gene ontology analysis performed by DAVID algorithm for DEX genes during fetal development, infancy and childhood, and adolescence and adulthood; **(A)** list of fetal-only, and **(B)** adolescence- and **(C)** adulthood-only terms.

### **Table S4 (associated with Figures 3 and 4): Co-expression modules 1-329**

**(A)** List of 122 modules corresponding to spatio-temporal patterns identified by weighted gene co-expression network analysis (WGCNA) with its functional interpretation and result of gene ontology analysis performed by DAVID algorithm; list of intra-modular genes and their intra-modular connectivity; and list of modules with gradient-like patterns: anterior-posterior, temporal, posterior perisylvian, and occipital. **(B)** List of 206 modules corresponding to spatio-temporal patterns identified by WGCNA with its functional interpretation and result of gene ontology analysis performed by DAVID algorithm; list of intra-modular genes and their intra-modular connectivity; and list of modules with region-specific enrichment in V1C and MFC.

### **Table S5 (associated with Figure 6): List of spike-ins RNAs**

**(A)** List of spike-in RNAs used for RNA-seq sample tagging and sequencing quality control. In total, 10 spike-in RNAs with different concentration were used. The length and GC content were provided for each spike-in RNA. **(B)** List of 16 pairs of spike-in RNAs used for sample tagging is provided.

## Supplemental Experimental Procedures

### 1. Introduction

In this Supplemental Experimental Procedures we provide further information regarding materials and methods. For a detailed description of the collection, dissection methods, and quality control assessments of post-mortem human brain, please refer to our previous study (Kang et al., 2011). We also make available additional data that were discussed in the main manuscript.

### 2. Neocortical Samples and Time Periods

For this study, we used a subset of a dataset previously reported (Kang et al., 2011). In that dataset, the full course of human brain development and adulthood was divided into 15 periods.

In the present study, we analyzed 11 areas of the neocortex (NCX) in periods 3-15, an interval during which all of the analyzed areas were represented (Kang et al., 2011; Table S2). The first 2 periods, which correspond to the embryonic and the first two weeks of the early fetal development, were not analyzed in the present study since they do not contain the same 11 areas from periods 3-15. As previously described, the localization of dissected samples was verified by histology in the postnatal brains and matched across fetal periods using the same anatomical landmarks (Kang et al., 2011). The complete list of periods and NCX samples, including corresponding putative functional areas, analyzed in this study can be found in the Table S2 and Figure 1, respectively.

Human post-mortem tissues analyzed in this study were obtained from several sources including the Human Fetal Tissue Repository at the Albert Einstein College of Medicine, the NICHD Brain and Tissue Bank for Developmental Disorders at the University of Maryland, the Laboratory of Developmental Biology at the University of Washington (supported by grant HD000836 from the Eunice Kennedy Shriver National Institute of Child Health and Human Development) and the JointMRC/Wellcome Trust Human Developmental Biology Resource (<http://hdbr.org>) at the IHG, Newcastle Upon Tyne (UK funding awards G0700089 and GR082557). All tissue was collected after obtaining parental or next of kin consent and with approval by the institutional review boards at the Yale School of Medicine and at each institution from which tissue specimens were obtained. Tissue was handled in accordance with ethical guidelines and regulations for the research use of human brain tissue set forth by the NIH (<http://bioethics.od.nih.gov/humantissue.html>) and the WMA Declaration of Helsinki (<http://www.wma.net/en/30publications/10policies/b3/index.html>).

### 3. Gene Expression Analyses

#### 3.1. Gene-level analysis

The expression levels for all core probe sets within an exon were averaged to obtain an expression value for the exon, and the median of all exons within one gene (transcript cluster) was used as the estimate of gene expression. To reduce the noise in the dataset and the false positives in the following differentially expressed genes investigations, we excluded genes with a log<sub>2</sub>-transformed expression value <6 in all samples. To consider a gene “expressed” in a particular area or at a particular time period, we required it to have a mean DABG  $P < 0.01$  in that NCX area. Analysis of gene expression using the core probe sets revealed that 13,956 of the 17,557 assayed genes (74.49%) were expressed in the NCX in at least one area of at least one period.

### **3.2. Principal component analysis**

The whole data set was subjected to the principal component analysis (PCA). The first and the second principal components (PC1 and PC2) were plotted and samples were colored by periods (Figure S1A). To explore the effects of confounders, we analyzed the first four principal components against RNA integrity number (RIN), post-mortem interval (PMI) and pH, and colored samples by periods. Negligible correlations were observed between expressed genes and the possible confounding factors.

### **3.3. Identification of spatial DEX genes**

Analysis of variance (ANOVA) was used to identify differentially expressed (DEX) genes across all regions of interest. Genes that were DEX in at least one NCX area were identified by using area as an ANOVA factor. In order to exclude the possibility that variation in RIN scores and PMI within the acceptable range might influence procedures, we included PMI and RIN as technical covariates within our ANOVA model of differential expression. Resulting *P*-values from ANOVA were corrected for multiple comparisons using the Benjamini and Hochberg false discovery rate (FDR) method (Benjamini and Hochberg, 1995). A conservative statistical threshold (FDR <0.01 and minimum fold difference >2 between NCX areas) was used to identify DEX genes. Genes that were not significantly expressed above background were excluded from ANOVA tests. A post-hoc Tukey's HSD (honestly significant difference) test was used to calculate differences between each pair of neocortical areas, in each period. The number of significant comparisons for each area, per period, was then used as the inter-areal (IA) DEX combinations number.

### **3.4. DEX analysis quality control**

#### **3.4.1. Subsampling**

Random subsamples were used to calculate the number of expressed and DEX genes. All samples were divided into three groups: prenatal, postnatal, and adult. The number of samples randomly chosen was calculated as  $\frac{3}{4}$  of the lowest number of samples contained within any of the three groups. For 100 trials, this fixed number of samples was randomly drawn from each group and the number of expressed or DEX genes was calculated using the selected subset of samples.

#### **3.4.2. Permutation test**

A permutation test was used to determine the dependence between group label and the mean number of expressed or DEX genes in the subsampling results. For each pair of groups (prenatal-postnatal, prenatal-adult, postnatal-adult), the test statistic was computed by subtracting the group with the smaller mean number from the group with the larger mean number. To calculate the null statistic, the group labels were shuffled, and mean difference was calculated retaining the same group order used to calculate the test statistic. The permutation was performed 999,999 times to generate the null distribution and calculate a one-sided *P*-value.

### **3.5. Transcriptome maturation**

#### **3.5.1 Maturation trajectories**

Period 14 is characterized by an adult-like pattern of brain functions (Kang et al., 2011), and can be considered as the period when cortical areas reach full maturation. We calculated the mean gene expression for each NCX area in this period and used it as the fully mature NCX reference for further comparisons. Additionally we used period 3 as a reference for early neocortical development. We then used the Pearson correlation of each sample to its areal reference as a measure of maturation.

The values of correlation were then smoothed to fit a trajectory by R function `smooth.spline`.

### 3.5.2. Maturation difference index

To better understand differences among areas in maturation, we calculated the average maturational trajectory for all areas. Areal deviations from the average maturational trajectory were used to calculate the maturational difference index for each area, in each period. The average maturational difference index was then calculated for prenatal and postnatal development.

### 3.6. Transcriptional profiling of neurobiological categories

Detailed information on gene selection and neurobiological categories are provided in ref. (Kang et al., 2011). To summarize the principle gene expression profile of each category, PCA was performed. The resulting first principal component (PC1) was plotted against logarithmic age in days, and a smooth curve was fitted by smoothing spline to display the developmental trajectories. For categories with only one gene, the expression level was used as PC1.

To compare the spatio-temporal patterns of genes in the same group, we plotted genes in each group individually and fitted the individual gene expression pattern by smoothing spline. To compare the developmental trajectories for neurodevelopmental processes (Figures S5 and S6), PC1 of each group was subjected to smoothing spline curve fitting. The fitted value  $\hat{y}_i$  was then scaled to 0 to 1. The range of fitted vector  $\hat{Y}$  was set to 1, and the scaled values were calculated as  $z_i = \frac{\hat{y}_i - \min(\hat{Y})}{\text{range}(\hat{Y})}$ . The scaled values were then plotted to represent the trajectory of each group with a measure of the percentage of changes. Furthermore, the average trajectory was calculated as a function of average value for all areas per period. Deviations from the average maturational trajectory were used to calculate the maturational difference index for all areas. The average maturational difference index was then calculated for prenatal and postnatal periods (3-7 and 8-15, respectively).

### 3.7. Weighted gene co-expression network analysis (WGCNA)

#### 3.7.1. Dataset filtering

WGCNA was applied to samples from periods 3-6 and periods 12-15, respectively. Since the analysis is sensitive to noise, only genes with  $\log_2$ -expression value greater than 6 in any of the sample and coefficient of variation (CV) greater than 0.05 were used for analysis.

#### 3.7.2. Network construction and module detection

Signed co-expression networks were built using the WGCNA package (Langfelder and Horvath, 2008, 2012) in R. For all genes included, a pair-wise correlation matrix was computed, and an adjacency matrix was calculated by raising the correlation matrix to a power. The power was set to 18 for both of Periods 3-6 and Periods 12-15, according to a scale-free topology criterion (Zhang and Horvath, 2005). For each pair of genes, a robust measure of network interconnectedness (topological overlap measure) was calculated based on the adjacency matrix. The topological overlap based dissimilarity was then used as input for average linkage hierarchical clustering. Modules were generated by hybrid dynamic tree-cutting. To obtain rare expression patterns, we set the minimum module size to 5 genes, `deepSplit` to 3, and the minimum height for merging modules to 0.15.

Each module was summarized by an eigengene, which is the first principal component of the scaled module expression. Thus, the module eigengene explained the maximum amount of variation of the module expression levels.

### 3.8. Gene ontology (GO) enrichment analysis

Functional enrichment was assessed using DAVID Bioinformatics Resources 6.7 (Huang et al., 2009a, b) (<http://david.abcc.ncifcrf.gov/>).

### 3.9. Spatio-temporal dynamics of co-expression modules

The expression patterns of modules were manually categorized based on module eigengenes. Modules that showed gradients in expression (Table S4A and Figure S2A-H) or region-specific expression (Table S4B and Figure S2I-L) were selected. To display the changes of expression across periods, the expression of genes in each selected module was scaled and the module expression was calculated by averaging the scaled expression across genes. The module expression was then plotted as a heatmap to show the change of gradients across periods. To demonstrate gradients for a selected period, the module expression in that period were plotted on a reference brain and labeled by gradients of colors.

### 3.10. Analysis of left-right bias in gene expression

Differences in gene expression between left and right hemispheres were analyzed by the combination of a sliding window algorithm, and a paired t-test. The sliding-window algorithm was used to detect left/right gene expression differences within a group of sequential periods. The window size was set to span 4 periods. For each window, a paired t-test was applied to determine if the expression level of a gene in left hemispheres was significantly different from the expression level in right hemispheres in the same area. The *P*-values from the t-tests were transformed to FDR using the Benjamini and Hochberg method (Benjamini and Hochberg, 1995). For each gene, the fold difference (log<sub>2</sub>-transformed) between left and right hemisphere samples in each region was also calculated. An FDR of 0.1 was used as a cutoff to identify genes that are DEX between left and right hemispheres in each window.

Using the same approach as in 3.5., we calculated the maturation trajectories of both hemispheres. The mean areal correlation of each period was calculated by hemisphere. The difference between hemispheres was then calculated for each area in each period. Bar plots were used to summarize the difference between hemispheres in prenatal and postnatal development (Figures 7A and B).

## 4. Transcriptome Validation

### 4.1. Quantitative real-time RT-PCR

Sequences of primers used in validation are as follows:

**ASAM** (forward: TGGCAGCGAATCCGAGAGAAAGA, reverse: TGCCTGCTGTGCACTGGTAC)  
**Asam** (forward: TGGCAGCGAATCCGGGAGAAGGA, reverse: TGCCTGCTGTGCACTGGTAG)  
**WNT7B** (forward: CCGCGAGAAGCAGGGCTACTACAA, reverse: CGTGGTCCAGCAGGTTTTGGTGGT)  
**Wnt7b** (forward: TGCTTTGGCGTCTGTACGTG, reverse: CTCTTGCAAGATGGCACGCTG)  
**NR2F2** (forward: CCATAGTCCTGTTACCTCAGA, reverse: AATCTGGTCGGCTGGTTG)  
**Nr2f2** (forward: CCATAGTCCTGTTACCTCAGA, reverse: AATCGCGTCGGCTGGTTG)  
**C13ORF38** (forward: TGAACGCCGTACATACCTAGCTGA, reverse: GGCAGTTGATCCACCT GTTGCCT)  
**C13orf38** (forward: TGAACGCCGTACATACCTAGCTGA, reverse: GGCAGTTGATCCATCTGT TGCCT)  
**KCNK12** (forward: TCGTGGGCACCGTGGTGTCA, reverse: AACAGGATGGTCCCAGCGCA)  
**Kcnk12** (forward: TCGTGGGCACCGTGGTGTCA, reverse: AACAGGATGGTACCGGCGCA)  
**WBSCR17** (forward: TGGTCTTCTGGATCCTGGCATGGA, reverse: GCCCCCACAGAGCCAT ACCTTG)  
**Wbscr17** (forward: CGGTCTTCTGGATCCTGGCATGGA, reverse: GCCCCCACAGAGCCATA CCTTG)  
**VAV3** (forward: TTGCTTGTGGTTTCTATGCAACGTG, reverse: TGCCTTCTCAGTCGGATCA GTGGTA)  
**Vav3** (forward: TTGCTTGTGGTTTCTATGCAACGTG, reverse: TGCCTTCTCAGTCGCATCAG CGGTA)  
**GABRQ** (forward: TTGGATATCGTTTTGGATGAACTA, reverse: CAGGATGAGCATTGAAGTT AAGC)  
**Gabrq** (forward: GGCACAGCTATGGTGTTCGCTT, reverse: TTCGGCACGGTTGCGGATTT)  
**TRPC3** (forward: TGTTCTGAAGGGCTGCCGGCTT, reverse: ACTCGCCTGAAAGTGACACCTGTGA)

**Trpc3** (forward: TCCCCAAATGCAGAAGGAGGC, reverse: CGTGGTGGCTGATTGAGAATGCTGT)  
**BAIAP3** (forward: AGGCCCTGTACACGGTGCTTTACC, reverse: GCAGTATGGGTCGCTGAAGCCGTT)  
**Baiap3** (forward: AGGCCCTGTACACAGTGCTTTACC, reverse: GCAGTATGGGTCACTGAAGCCATT)  
**RPL32** (forward: CAACATTGGTTATGGAAGCAACA, reverse: TGACGTTGTGGACCAGGAACT)  
**Rpl32** (forward: CAACATTGGTTATGGGAGCAACA, reverse: TGACGTTGTGGACCAGGAACT).

qRT-PCR results were shown in radar charts, which were plotted using Origin 8.6 plotting software. Gradient-like patterns of gene expression (Fig. 3I-L) were shown by grouping areas per lobe: frontal (MFC, OFC, DFC, VFC, M1C), parietal (S1C, IPC), temporal (STC, A1C, ITC), and occipital (V1C). Region specific/enriched patterns of genes (Fig. 4F-I) were plotted by grouping regions of interest against all other areas combined. Also, we show the expression values of each area using radar charts (Figure S3) and we compared patterns of expression between the species, calculating Pearson's correlation coefficient for brains with matched age.

## 4.2. Immunohistochemistry

For validation studies, 22PCW human brain tissue samples were fixed in 4% PFA for 2 days at 4 °C. Tissue sections were incubated in 1% hydrogen peroxide/PBS to quench endogenous peroxidase activity. Sections were washed in PBS (3 x 15 min) and incubated in blocking solution containing 5% (v/v) normal donkey serum (Jackson ImmunoResearch Laboratories), 1% (w/v) bovine serum albumin, and 0.4% (v/v) Triton X-100 in PBS for 1 h at room temperature. Primary antibodies - WNT7B (R & D SYSTEMS, AF3460) and NR2F2 (Abcam, ab50487) – were diluted (WNT7B 1:100, NR2F2 1:100) in blocking solution and incubated with tissues sections overnight at 4 °C. Sections were washed with PBS (3 x 15 min) prior to being incubated with the appropriate biotinylated secondary antibodies (Jackson ImmunoResearch Labs) for 1.5 h at room temperature. All secondary antibodies were raised in donkey and diluted at 1:200 in blocking solution. Sections were subsequently washed in PBS and incubated with avidin-biotin-peroxidase complex (Vectastain ABC Elite kit; Vector Laboratories) for 1 h at room temperature. Finally, sections were washed in PBS (3 x 15 min) and signals were developed using a DAB peroxidase substrate kit according to the manufacturer's protocol (Vector Laboratories). Following washes in PBS, sections were mounted on Superfrost Plus charged slides, dried, dehydrated, and cover slipped with Permount (Fisher Scientific Co.). Sections were digitized using AxioTome (Zeiss). Digitized images were assembled in Zeiss Zen, Adobe Photoshop and Illustrator.

## 5. Dissection of Rhesus Macaque (*Macaca mulatta*) Neocortical Areas

We performed qRT-PCR using RNA isolated from homologous areas of the rhesus macaque (*Macaca mulatta*) NCX at equivalent developmental periods using a mathematical model to translate neurodevelopmental time across species (Clancy et al., 2007). The list of macaque brains used in this study is listed in Table S1C. Macaque experiments were carried out in accordance with a protocol approved by Yale University's Committee on Animal Research and NIH guidelines. All brains were dissected using the same protocol used for human specimens. Sex and age of monkeys are listed in Table S4C. Areas were sampled according to ref. (Saleem and Logothetis, 2007). An overview of dissected areas can be found in Figure 1.

## 6. mRNA-sequencing

### 6.1. Library preparation and sequencing

The mRNA-Seq Sample Kit (Illumina) was used to prepare cDNA libraries per manufacturer instructions with some modifications. Briefly, polyA RNA was purified from 1 to 5 µg of total RNA

using (dT) beads. Quaint-IT RiboGreen RNA Assay Kit (Invitrogen) was used to quantitate purified mRNA with the NanoDrop 3300. Following mRNA quantitation, spike-in RNAs that were synthesized by the External RNA Control Consortium (ERCC) and were a generous gift of Dr. Mark Salit at The National Institute of Standards and Technology (NIST), were added to the mRNA for tagging the sample as well as for controlling sequencing error rates, which is not influenced by SNPs (Jiang et al., 2011). The mixture of mRNA and spike-in RNAs were subjected to fragmentation, reverse transcription, end repair, 3' end adenylation, and adapter ligation to generate libraries of short cDNA molecules. The libraries were size selected at 200 to 250 bp by gel excision, followed by PCR amplification and column purification. The final product was assessed for its size distribution and concentration using Bioanalyzer DNA 1000 Kit. For sequencing, we used Illumina Genome Analyzer IIx (GAIIx) by loading one sample per lane. The library was diluted to 10 nM in EB buffer and then denatured using the Illumina protocol. The denatured libraries were diluted to 12 pM, followed by cluster generation on a single-end GAIIx flow cell (v4) using an Illumina cBOT, according to the manufacturer's instructions. The flow cell was run for 76 cycles using a single-read recipe (v4 sequencing kits) according to the manufacturer's instructions.

## **6.2. mRNA sequencing alignment and expression quantification pipeline**

An analysis pipeline for mapping and annotation was developed in-house using the RSEQtools framework (Habegger et al., 2011). Briefly, the sequenced reads were processed and quality filtered based on CASAVA 1.7 pipeline, then aligned to the references (human genome: hg19, GRCh37 and for spike-in RNAs) using Tophat version 1.3.1 (Trapnell et al., 2009). The gtf format annotation, GENCODE (version 3c), was additionally provided to improve the mapping quality of exon-exon junction reads. After the reads were mapped to the reference sequences, the expression level of genes, exons and spike-in RNAs was measured in the commonly used units of RPKM (reads per kilobase of exon model per million mapped reads) (Mortazavi et al., 2008). SAMtools and RSEQtools were used to perform this task (Habegger et al., 2011; Li et al., 2009). We restricted the downstream analysis to using uniquely mapped reads because of the uncertainty of the reads with multiple mappable sites. In addition, mitochondrial reads were excluded due to their deep coverage and the large variation across different individuals. After filtering, RPKM values were computed using a composite model of a gene, which is defined as a union of all exonic nucleotides across all of its transcripts from GENCODE.

## **6.3. Quality assessment**

We used different pairs of spike-in RNAs to tag different samples (Table S5). The pair of spike-in RNAs was used to identify any possible sample swaps from the period of library preparation to sample loading on the GAIIx. In addition, three common spike-in RNAs combined with these two spike-in RNAs together served another purpose, i.e., calculation of sequence error rate. Since we know the sequence of the spike-in RNAs, mismatches between the sequenced reads and the reference spike-in RNAs were used to estimate sequencing error rate. We plotted the dependence between the percentage of mismatches and the sequencing cycles, and found low sequencing error rates (median values <5%) as well as the expected increase towards the end of the sequencing cycles (Figure S7A).

We also analyzed technical replicates to estimate different batch or different lane effect. We ran 5 technical replicates and analyzed each sample to calculate RPKMs. The high pairwise gene/exon expression correlations with low variation suggested minor effects by processing the same set of RNA samples in different lanes and batches (Spearman correlation,  $r = 0.98 \pm 0.0067$  for genes and  $0.93 \pm 0.0081$  for exons,  $N = 5$ ).

Using the same 5 technical replicates, we further simulated the dependence between sequencing depth and coverage of the transcriptome. Continuous numbers of reads (1M, 2M, ..., 20M, M indicates million) randomly sampled from one lane, as well as the combinations of lanes (one,

two, three, four, and five lanes) were built to represent possible sequencing depths. Resulting RPKM scores were classified into two groups:  $RPKM \geq 1$  for highly expressed genes and  $0 < RPKM < 1$  for lowly expressed genes. It was shown that the discovery rate of the highly expressed genes/exons was minimally affected by the sequencing depth, in contrast to the lowly expressed genes/exons (Figure S7B). This result suggested that more lanes were required for sufficient identification of genes/exons with low level expression. On the other hand, we showed the effect of sequencing depth on the genes/exons expression quantification (Figure S7C). We used the following procedures to estimate expression variation of genes and exons: (1) Genes/exons were classified into two groups; (2) The genes/exons expression of the five combined lanes was chosen as reference; (3) In each simulated sequencing depth, the relative ratios to the reference for the genes/exons expression were calculated. The distribution of the log<sub>2</sub>-transformed relative ratios for genes and exons in each simulated sequencing depth showed that expression quantification settles on smaller deviations once the sequencing depth reaches sub-million reads, or more confidently, 10M reads (Figure S7C). Together, the simulation suggested that at least 10M reads were necessary to adequately cover the human brain transcriptome although more lanes resulted in improved coverage of genes with low level expression. All of our samples passed this threshold, leaving enough confidence in calling differential gene expression.

#### **6.4. Correlation of Exon Array and RNA-seq**

We compared gene expression between both Exon Array and RNA-seq. Pearson correlation for all comparable pairs showed  $0.65 \pm 0.08$ . High correlations between two different platforms indicated these results are highly reproducible and less variable in each platform (Figure S7D).

#### **6.5. Analysis of left-right bias in gene expression**

We computed left and right biased genes in STC utilizing paired t-test against fetal, infancy to adolescence, and adult individuals so that each group contains 4 pairs of left and right comparison. For each group, a paired t-test was applied to determine if the expression level of a given gene in one hemisphere was significantly different from that in the other hemisphere. The *P*-values from the t-tests were transformed to FDRs using the Benjamini and Hochberg method (Benjamini and Hochberg, 1995). For each gene, the fold difference (log<sub>2</sub>-transformed) between left and right hemisphere samples in each region was also calculated. An FDR of 0.1 was used as a cutoff to identify genes that are DEX between left and right hemispheres in each group (Figure 6C).

### **Supplemental References**

Habegger, L., Sboner, A., Gianoulis, T.A., Rozowsky, J., Agarwal, A., Snyder, M., and Gerstein, M. (2011). RSEQtools: a modular framework to analyze RNA-Seq data using compact, anonymized data summaries. *Bioinformatics* 27, 281-283.

Jiang, L., Schlesinger, F., Davis, C.A., Zhang, Y., Li, R., Salit, M., Gingeras, T.R., and Oliver, B. (2011). Synthetic spike-in standards for RNA-seq experiments. *Genome Res* 21, 1543-1551.

Li, H., Handsaker, B., Wysoker, A., Fennell, T., Ruan, J., Homer, N., Marth, G., Abecasis, G., Durbin, R., and Genome Project Data Processing, S. (2009). The Sequence Alignment/Map format and SAMtools. *Bioinformatics* 25, 2078-2079.

Mortazavi, A., Williams, B.A., McCue, K., Schaeffer, L., and Wold, B. (2008). Mapping and quantifying mammalian transcriptomes by RNA-Seq. *Nat Methods* 5, 621-628.

Saleem, K.S., and Logothetis, N. (2007). A combined MRI and histology atlas of the rhesus monkey brain in stereotaxic coordinates (London ; Burlington, MA: Academic).

Trapnell, C., Pachter, L., and Salzberg, S.L. (2009). TopHat: discovering splice junctions with RNA-Seq. *Bioinformatics* 25, 1105-1111.

Zhang, B., and Horvath, S. (2005). A general framework for weighted gene co-expression network analysis. *Stat Appl Genet Molec Biol* 4, Article17.